The dynamics of the quasielastic ^{16}O$(e,e'p)$ reaction at $Q^2 = 0.8$ (GeV/c)^2

K.G. Fissum,[1,*] B.D. Anderson,[2] K.A. Aniol,[3] L. Auerbach,[4] F.T. Baker,[5] J. Berthot,[6] W. Bertozzi,[1] P.-Y Bertin,[6] L. Bimbot,[7] W.U. Boeglin,[8] E.J. Brash,[9] V. Breton,[6] H. Breuer,[10] E. Burtin,[11] J.R. Calarco,[12] L. Cardman,[13] G.D. Cates,[14] C. Cavata,[11] C.C. Chang,[10] J.-P. Chen,[13] E. Cisbani,[15] D.S. Dale,[16] R. De Leo,[17] A. Deur,[6] B. Diederich,[18] P. Djawotho,[19] J. Domingo,[13] B. Doyle,[16] J.-E. Ducret,[11] M.B. Epstein,[3] L.A. Ewell,[10] J.M. Finn,[19] H. Fonvieille,[6] B. Frois,[11] S. Frullani,[15] J. Gao,[1] F. Garibaldi,[15] A. Gasparian,[16,20] S. Gilad,[1] R. Gilman,[13,21] A. Glamazdin,[22] C. Glashausser,[21] J. Gomez,[13] V. Gorbenko,[22] T. Gorringe,[16] F.W. Hersman,[12] R. Holmes,[23] M. Holtrop,[12] N. d'Hose,[11] C. Howell,[24] G.M. Huber,[9] C.E. Hyde-Wright,[18] M. Iodice,[15] C.W. de Jager,[13] S. Jaminion,[6] M.K. Jones,[19] K. Joo,[25] C. Jutier,[6,18] W. Kahl,[23] S. Kato,[26] J.J. Kelly,[10] S. Kerhoas,[11] M. Khandaker,[27] M. Khayat,[2] K. Kino,[28] W. Korsch,[16] L. Kramer,[8] K.S. Kumar,[14] G. Kumbartzki,[21] G. Laveissière,[6] A. Leone,[29] J.J. LeRose,[13] L. Levchuk,[22] M. Liang,[13] R.A. Lindgren,[25] N. Liyanage,[1] G.J. Lolos,[9] R.W. Lourie,[30] R. Madey,[2,13,20] K. Maeda,[28] S. Malov,[21] D.M. Manley,[2] D.J. Margaziotis,[3] P. Markowitz,[8] J. Martino,[11] J.S. McCarthy,[25] K. McCormick,[18] J. McIntyre,[21] R.L.J. van der Meer,[9] Z.-E. Meziani,[4] R. Michaels,[13] J. Mougey,[31] S. Nanda,[13] D. Neyret,[11] E.A.J.M. Offermann,[13] Z. Papandreou,[9] C.F. Perdrisat,[19] R. Perrino,[29] G.G. Petratos,[2] S. Platchkov,[11] R. Pomatsalyuk,[22] D.L. Prout,[2] V.A. Punjabi,[27] T. Pussieux,[11] G. Quéméner,[19] R.D. Ransome,[21] O. Ravel,[6] Y. Roblin,[6] R. Roche,[32] D. Rowntree,[1] G.A. Rutledge,[19] P.M. Rutt,[21] A. Saha,[13] T. Saito,[28] A.J. Sarty,[32] A. Serdarevic-Offermann,[9] T.P. Smith,[12] A. Soldi,[33] P. Sorokin,[22] P. Souder,[23] R. Suleiman,[2] J.A. Templon,[5] T. Terasawa,[28] L. Todor,[18] H. Tsubota,[28] H. Ueno,[26] P.E. Ulmer,[18] G.M. Urciuoli,[15] P. Vernin,[11] S. van Verst,[1] B. Vlahovic,[33] H. Voskanyan,[34] J.W. Watson,[2] L.B. Weinstein,[18] K. Wijesooriya,[19] R. Wilson,[35] B. Wojtsekhowski,[13] D.G. Zainea,[9] V. Zeps,[16] J. Zhao,[1] and Z.-L. Zhou[1]

(The Jefferson Lab Hall A Collaboration)

J.M. Udías and J.R. Vignote

Universidad Complutense de Madrid, E-28040 Madrid, Spain

and J. Ryckebusch and D. Debruyne

Ghent University, B-9000 Ghent, Belgium

[1] *Massachusetts Institute of Technology, Cambridge, Massachusetts, 02139, USA*
[2] *Kent State University, Kent, Ohio, 44242, USA*
[3] *California State University, Los Angeles, California, 90032, USA*
[4] *Temple University, Philadelphia, Pennsylvania, 19122, USA*
[5] *University of Georgia, Athens, Georgia, 30602, USA*
[6] *Université Blaise Pascal/IN2P3, F-63177 Aubière, France*
[7] *Institut de Physique Nucléaire, F-91406 Orsay, France*
[8] *Florida International University, Miami, Florida, 33199, USA*
[9] *University of Regina, Regina, Saskatchewan, Canada, S4S 0A2*
[10] *University of Maryland, College Park, Maryland, 20742, USA*
[11] *CEA Saclay, F-91191 Gif-sur-Yvette, France*
[12] *University of New Hampshire, Durham, New Hampshire, 03824, USA*
[13] *Thomas Jefferson National Accelerator Facility, Newport News, Virginia, 23606, USA*
[14] *Princeton University, Princeton, New Jersey, 08544, USA*
[15] *INFN, Sezione Sanitá and Istituto Superiore di Sanitá, Laboratorio di Fisica, I-00161 Rome, Italy*
[16] *University of Kentucky, Lexington, Kentucky, 40506, USA*
[17] *INFN, Sezione di Bari and University of Bari, I-70126 Bari, Italy*
[18] *Old Dominion University, Norfolk, Virginia, 23529, USA*
[19] *College of William and Mary, Williamsburg, Virginia, 23187, USA*
[20] *Hampton University, Hampton, Virginia, 23668, USA*
[21] *Rutgers, The State University of New Jersey, Piscataway, New Jersey, 08854, USA*
[22] *Kharkov Institute of Physics and Technology, Kharkov 310108, Ukraine*
[23] *Syracuse University, Syracuse, New York, 13244, USA*
[24] *Duke University, Durham, North Carolina, 27706, USA*
[25] *University of Virginia, Charlottesville, Virginia, 22901, USA*
[26] *Yamagata University, Yamagata 990, Japan*
[27] *Norfolk State University, Norfolk, Virginia, 23504, USA*
[28] *Tohoku University, Sendai 980, Japan*
[29] *INFN, Sezione di Lecce, I-73100 Lecce, Italy*

[30] State University of New York at Stony Brook, Stony Brook, New York, 11794, USA
[31] Institut des Sciences Nucléaires, F-38026 Grenoble, France
[32] Florida State University, Tallahassee, Florida, 32306, USA
[33] North Carolina Central University, Durham, North Carolina, 27707, USA
[34] Yerevan Physics Institute, Yerevan 375036, Armenia
[35] Harvard University, Cambridge, Massachusetts, 02138, USA
(Dated: October 7, 2002)

The physics program in Hall A at Jefferson Laboratory commenced in the summer of 1997 with a detailed investigation of the ^{16}O$(e,e'p)$ reaction in quasielastic, constant (q,ω) kinematics at $Q^2 \approx 0.8$ (GeV/c)^2, $|\vec{q}| \approx 1$ GeV/c, and $\omega \approx 445$ MeV. Use of a self-calibrating, self-normalizing thin-film water target enabled a systematically rigorous measurement. Five-fold differential cross sections for the removal of protons from the $1p$-shell have been obtained for $0 < P_{\rm miss} < 350$ MeV/c. Six-fold differential cross sections for $0 < E_{\rm miss} < 100$ MeV were obtained for $0 < P_{\rm miss} < 350$ MeV/c. These results have been folded to extract the A_{LT} asymmetry and the R_L, R_T, R_{L+TT}, and R_{LT} response functions over a large range of $E_{\rm miss}$ and $P_{\rm miss}$. Fully relativistic distorted wave impulse approximation calculations describe the $1p$-shell data well, and at $P_{\rm miss} > 300$ MeV/c, dynamical relativistic effects are indicated by the observed structure in A_{LT}. For $E_{\rm miss} > 25$ MeV, calculations which include isobar currents, pion exchange currents, and short-range correlations account for the shape and the transverse nature of the data but only half the magnitude of the measured cross section. For $25 < E_{\rm miss} < 50$ MeV and $P_{\rm miss} \approx 60$ MeV/c, proton knockout from the $1s_{1/2}$-state dominates; however, this single-particle behavior is increasingly masked by more complicated processes for larger $P_{\rm miss}$.

PACS numbers: 25.30.Fj, 24.70.+s, 27.20.+n

I. INTRODUCTION

Exclusive and semi-exclusive $(e,e'p)$ in quasielastic kinematics [101] has long been used as a precision tool for the study of nuclear electromagnetic response [1–3]. Cross section data have provided information used to study the single-nucleon aspects of nuclear structure and the wave functions of protons bound inside the nucleus, as well as to search for non-nucleonic degrees-of-freedom and to stringently test nuclear theories. Response function separations [102] have been used to extract detailed information about the different reaction mechanisms contributing to the cross sections, since they are selectively sensitive to differenct aspects of the nuclear current.

Early $(e,e'p)$ energy and momentum distributions were measured by Amaldi *et al.* [4]. These results, and those which followed [1, 3, 5], were interpreted within the framework of single-particle knockout from nuclear valence states, even though the measured cross sections were as much as 40% lower than expected. The first relativistic calculations for bound-state proton knockout via $(e,e'p)$ were performed by Picklesimer and Van Orden [6, 7]. Such Distorted Wave Impulse Approximation (DWIA) calculations are generally accepted to be more accurate at higher Q^2, since quasielastic $(e,e'p)$ is expected to be dominated by single-particle interactions in this regime of four-momentum transfer.

Other aspects of the structure as well as the reaction mechanism have generally been studied at higher $E_{\rm miss}$. While it is experimentally convenient to perform measurements spanning the two excitation regions simultaneously, there is unfortunately no coherent theoretical picture that uniformly explains the data for all missing energy. In fact, the theoretical tools used to describe the two regimes are very different. Within our present understanding, the regions are related mainly by the transfer of strength from the valence states to higher $E_{\rm miss}$ [8].

The nucleus ^{16}O has long been a favorite for theorists, since it has a doubly closed-shell whose structure is thus easier to model than other nuclei. It is also a convenient target for experimentalists. While the knockout of $1p$-shell protons from ^{16}O has been studied extensively in the past at lower Q^2, few data were available at higher missing energies at the time this experiment was conceived.

1. $1p$-shell knockout

The knockout of $1p$-shell protons in ^{16}O$(e,e'p)$ was studied by Bernheim *et al.* [9] and Chinitz *et al.* [10] at Saclay, Spaltro *et al.* [11] and Leuschner *et al.* [12] at NIKHEF-K, and Blomqvist *et al.* [13] at Mainz at four-momentum transfers $Q^2 < 0.4$ (GeV/c)^2. In these experiments, the cross sections were measured as a function of $P_{\rm miss}$, and spectroscopic factors (relating how much lower the measured cross sections were than expected) were extracted. These published spectroscopic factors ranged between 0.5 and 0.7, but Kelly [1, 2] has demonstrated that the Mainz [13] data suggest a significantly smaller normalization factor (see also Table VI). Chinitz *et al.* [10] and Spaltro *et al.* [11] also extracted R_{LT},

*Corresponding author. Present address: Department of Physics, University of Lund, Box 118, SE-221 00 Lund, Sweden; Electronic address: kevin.fissum@nuclear.lu.se

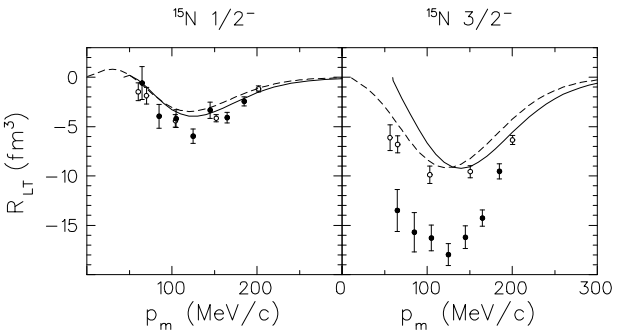

FIG. 1: Longitudinal-transverse interference responses as a function of $P_{\rm miss}$ for the $1p$-shell of ^{16}O. Open (filled) circles were extracted from quasielastic data obtained by Chinitz *et al.* [10] (Spaltro *et al.* [11]) at $Q^2 = 0.3$ (GeV/c)^2 ($Q^2 = 0.2$ (GeV/c)^2). The calculations [14] are based on fits to distorted momentum distributions measured in parallel kinematics by Leuschner *et al.* [12]. MAYBE GET UDIAS FIGURE INSTEAD.

the longitudinal-transverse interference response, at both $Q^2 = 0.3$ (GeV/c)^2 and 0.2 (GeV/c)^2 respectively. Their measurements for the $1p_{1/2}$-state agree, but those for the $1p_{3/2}$-state disagree dramatically. DWIA calculations by Kelly [14] based on fits to distorted momentum distributions measured in parallel kinematics at NIKHEF-K [12] are consistent with the data of Chinitz *et al.* [10] (see Figure 1).

Recent relativistic calculations by Udías *et al.* [15–19] suggest that for removal of $1p$-shell protons in ^{16}O$(e,e'p)$, the longitudinal-transverse interference response function R_{LT} and the left-right asymmetry A_{LT} [103] are both very sensitive to the dynamical enhancement of the distorted (with respect to the undistorted or free) lower components of the Dirac spinors. These calculations predict that proper inclusion of these dynamical relativistic effects is needed to reproduce both A_{LT} and R_{LT}, particularly at $P_{\rm miss} > 300$ MeV/c.

2. *Higher missing energies*

Not many data are available for ^{16}O$(e,e'p)$ at higher missing energies, and much of what we know about this excitation region is from studies of other nuclei, mainly from ^{12}C. At MIT-Bates [20–24], in a series of ^{12}C$(e,e'p)$ experiments performed at missing energies above the two-nucleon emission threshold, cross sections much larger than those predicted by single-particle knockout models were measured. In particular, Ulmer *et al.* [20] identified a marked increase in the transverse-longitudinal difference [104]. A similar increase has subsequently been observed by Lanen *et al.* [25] for ^{6}Li, by van der Steenhoven *et al.* [26] for ^{12}C, and most recently by Dutta *et al.* for ^{12}C [27], ^{56}Fe, and ^{197}Au [28]. The transverse increase exists over a large range of four-momentum transfers, though the excess at lower

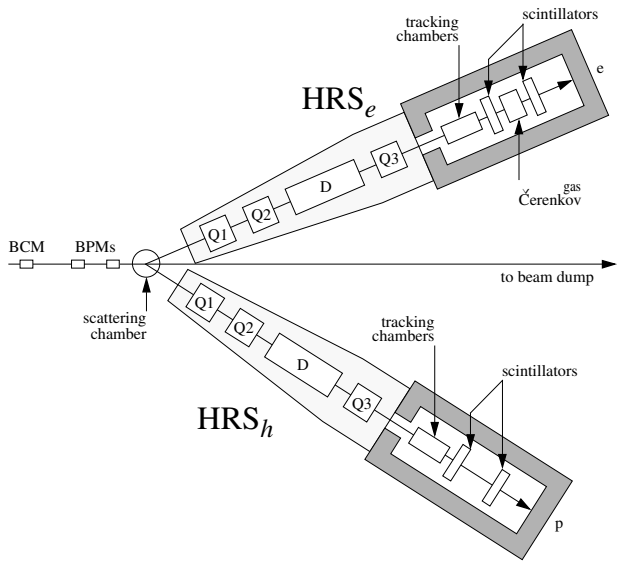

FIG. 2: Hall A at Jefferson Lab at the time of this experiment. The electron beam passed through a beam current monitor (BCM) [37] and beam position monitors (BPMs) [38, 39] before striking a waterfall target [40] located in the scattering chamber. Scattered electrons were detected in the HRS$_e$, while knocked-out protons were detected in the HRS$_h$. Non-interacting electrons were dumped. The spectrometers were free to rotate about the central pivot.

$P_{\rm miss}$ seems to decrease with increasing Q^2 [28]. Theoretical attempts to explain the data at high $E_{\rm miss}$ using two-body knockout models [29–31] coupled to final-state interactions (FSI) do not succeed. Even for quasielastic kinematics, cross sections at high $E_{\rm miss}$ are associated with significant contributions from non-single-particle processes.

II. EXPERIMENT

This experiment [32, 33] was the inaugural physics investigation performed in Hall A [34] (the High Resolution Hall) at the Thomas Jefferson National Accelerator Facility (JLab) [35]. An overview of the experiment apparatus in the Hall at the time of this measurement is shown in Figure 2. For a thorough discussion of the experimental infrastructure and its capabilities, the interested reader is directed to [36]. For the sake of completeness, a subset of the aforementioned information is presented here.

A. Electron beam

Unpolarized 70 μA continuous electron beams with energies of 0.843, 1.643, and 2.442 GeV (corresponding to different virtual photon polarizations) and a typical $\pm 4\sigma$ energy spread of 0.01% were used for this experiment (see Table I). Subsequent analysis of the data demonstrated

TABLE I: Experiment kinematics. These quasielastic parameters were established within a constant center-of-mass energy framework. At each beam energy, $|\vec{q}| \approx 1$ GeV/c. The angles $\theta_{pq} = 0, \pm 2.5, \pm 8, \pm 16$, and $\pm 20^\circ$ correspond to central missing momenta of 53, 60, 148, 280, and 345 MeV/c, respectively.

$E_{\rm beam}$ (GeV)	θ_e ($^\circ$)	virtual photon polarization	θ_{pq} ($^\circ$)
0.843	100.76	0.21	0, 8, 16
1.643	37.17	0.78	0, $\pm$8
2.442	23.36	0.90	0,$\pm$2.5, $\pm$8, $\pm$16, $\pm$20

that the actual beam energies were within 0.3% of the nominal values [41].

The typical laboratory horizontal (vertical) $\pm 4\sigma$ beam extent at the target was 0.5 mm (0.1 mm) . Beam current monitors [37] (calibrated using an Unser monitor [42–44]) were used to determine the total charge delivered to the target to an accuracy of 2% [45]. Beam position monitors (BPMs) [38, 39] were used to ensure the location of the beam at the target was no more than 0.2 mm from the beamline axis, and that the instantaneous angle between the beam and the beamline axis was no larger than 0.15 mrad. The readout from the BCM and BPMs was continuously passed into the data stream [46]. Non-interacting electrons were dumped in a well-shielded, high-power beam dump [47] located roughly 30 m from the target.

B. Target

A waterfall target [40] positioned inside a scattering chamber located at the center of the Hall provided the H_2O used for this study of ^{16}O. The target canister was a rectangular box 20 cm long × 15 cm wide × 10 cm high containing air at atmospheric pressure. The beam entrance (exit) windows to this canister were 50 μm (75 μm) gold-plated beryllium foils. Inside the canister, three thin, parallel water films served as targets. This three-film configuration was superior to a single film 3× thicker because it reduced the target-associated multiple scattering and energy loss. The films were defined by 2 mm × 2 mm stainless-steel posts. Each film was separated by 25 mm along the direction of the beam, and was rotated such that the normal to the film surface made an angle of 30° with respect to the beam direction. This geometry ensured that particles originating from any given film would not intersect any other film on their way into the spectrometers.

The thickness of the films could be changed by varying the speed of the water flow through the target circuit via a pump. The average film thicknesses were fixed at (130 ± 2.5%) mg/cm^2 along the direction of the beam throughout the experiment, which provided a good trade-off between resolution and target thickness. The thickness of the central water film was determined by comparing $^{16}\mathrm{O}(e,e')$ cross sections measured at $|\vec{q}| = 330$ MeV/c obtained from both the film and a (155 ± 1.5%) mg/cm^2 BeO target foil placed in a solid target ladder mounted beneath the target canister. The thicknesses of the side films were determined by comparing the concurrently measured $^1\mathrm{H}(e,e)$ cross sections obtained from these side films to that obtained from the central film. Instantaneous variations in the target film thicknesses were monitored throughout the entire experiment by continuously measuring the $^1\mathrm{H}(e,e)$ cross sections. The scattered electrons and knocked-out protons passed through the 25 μm thick stainless-steel canister side windows on their way into the spectrometers, depositing roughly 200 keV.

TABLE II: Results of the optics commissioning measurements.

parameter	resolution (FWHM)	reconstruction accuracy
out-of-plane angle	6.00 mrad	±0.60 mrad
in-plane angle	2.30 mrad	±0.23 mrad
$y_{\rm target}$	2.00 mm	±0.20 mm
$\Delta p/p$	2.5×10^{-4}	-

C. Spectrometers and detectors

The base apparatus used in the experiment was a pair of optically identical 4 GeV/c superconducting High Resolution Spectrometers (HRS) [48]. These spectrometers have a nominal 9% momentum bite and a FWHM momentum resolution $\Delta p/p$ of roughly 10^{-4}. The nominal laboratory horizontal (vertical) angular acceptance is ±25 (±50) mrad. Scattered electrons were detected in the Electron Spectrometer (HRS$_e$), and knocked-out protons were detected in the Hadron Spectrometer (HRS$_h$) (see Figure 2). Before the experiment, the absolute momentum calibration of the spectrometers was determined to $\Delta p/p = 1.5 \times 10^{-3}$ [41]. Before and during the experiment, both the optical properties and acceptances of the spectrometers were studied [49]. Some optical parameters are presented in Table II.

During the experiment, the locations of the spectrometers were surveyed to an accuracy of 0.3 mrad at every angular location [50]. The status of the magnets was continuously monitored and logged [46].

The detector packages were located in a well-shielded detector huts built on decks located above each spectrometer (approximately 25 m from the target and 15 m above the floor of the Hall). The bulk of the instrumentation electronics were also located in these huts, and operated remotely from the Counting House. The HRS$_e$ detector package consisted of a pair of trigger scintillator planes [51] used to create triggers, a Vertical Drift Chamber (VDC) package [52, 53] used for particle tracking,

and a Gas Čerenkov counter [54] used to distinguish between π^- and electron events. Identical elements, except for the Gas Čerenkov counter, were also present in the HRS_h detector package. The status of the various detector subsystems was continuously monitored and logged [46]. The individual operating efficiencies of each of these three devices was >99%.

D. Electronics and data acquisition

For a given spectrometer, a coincidence between signals from the two trigger scintillator planes indicated a 'single-arm' event. Simultaneous HRS_e and HRS_h singles events were recorded as 'coincidence' events. The basic trigger logic [55] allowed the proportion of single-arm events written to the data stream to be varied by remotely setting prescalers. Enough HRS_e singles were taken for a 1% statistics $^1\mathrm{H}(e,e)$ cross section measurement at each kinematics. Each spectrometer had its own VME crate (for scalers) and FASTBUS crate (for ADCs and TDCs). The crates were managed by readout controllers (ROCs). In addition to overseeing the state of the run, a trigger supervisor (TS) generated the triggers which caused the ROCs to read out the crates on an event-by-event basis. The VME (scaler) crate was also read out every ten seconds. An event builder (EB) collected the resulting data shards into events. An analyzer/data distributer (ANA/DD) analyzed and/or sent these events to the disk of the data acquisition computer. The entire data acquistion system was managed using the software toolkit CODA [56].

Typical scaler events were about 0.5 kb in length. Typical single-arm events were also about 0.5 kb, while typical coincidence events were about 1.0 kb. The acquisition deadtime η was monitored by measuring the TS output-to-input ratio for each event type. The event rates were set by varying the prescale factors and the beam current such that the DAQ computer was busy at the most only 20% of the time. This resulted in a relatively low event rate (kHz), at which the electronics deadtime was <1%. Online analyzers [57] were used to monitor the quality of the data as it was taken. Eventually, the data were transferred to magnetic tape. The ultimate data analysis was performed on a LINUX CPU farm [58] at the Massachusetts Institute of Technology using the analysis package ESPACE [59].

III. ANALYSIS

The interested reader is directed to [60, 61] for a complete discussion of the data analysis. For the sake of completeness, a subset of the aforementioned information is presented here.

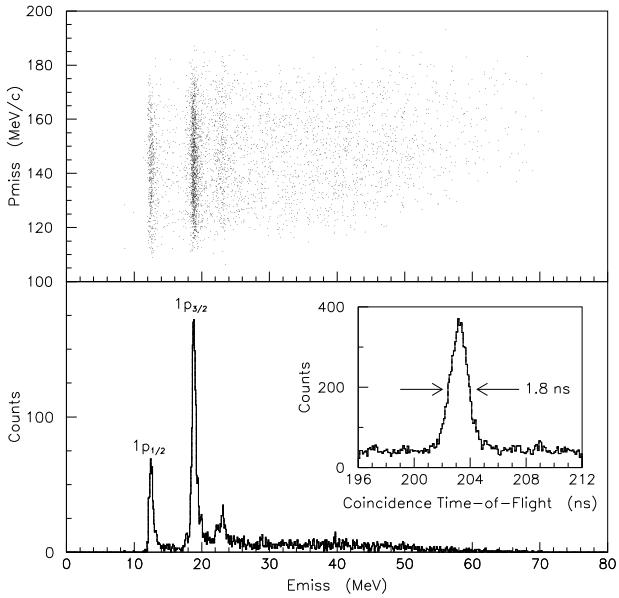

FIG. 3: Typical yield spectrum obtained at $E_{\mathrm{beam}} = 0.843$ GeV and $\theta_{pq} = +8^\circ$, corresponding to $P_{\mathrm{miss}} \approx 148$ MeV/c. Pion rejection has been performed, and all timing corrections have been applied. The top panel shows a scatterplot of P_{miss} versus E_{miss}. The dark vertical bands project into the peaks located at 12.1 (18.3) MeV in the bottom panel. These peaks correspond to protons knocked-out of the $1p_{1/2}$- ($1p_{3/2}$-) state of ^{16}O. The missing energy resolution was roughly 0.9 MeV FWHM, which did not allow for separation of the $2s_{1/2}1d_{5/2}$-doublet located at $E_{\mathrm{miss}} = 17.4$ MeV from the $1p_{3/2}$-state at 18.3 MeV. The bump located at roughly 23 MeV is a negative-parity doublet which was not investigated. The insert shows the corresponding optimized coincidence Time-of-Flight peak which has a FWHM of 1.8 ns. The signal-to-noise ratio was about 8:1 in these kinematics.

A. Timing corrections and particle identification

Identification of coincidence $(e,e'p)$ events was in general a straightforward process. Software corrections were applied to remove timing variations induced by the trigger scintillator circuit and thus sharpen all Time-of-Flight (ToF) peaks. These included corrections to proton flight times due to variations in the proton kinetic energies, and corrections for variations in the electron and proton path lengths through the spectrometers. Pion rejection was performed using a ToF cut for π^+s in the HRS_h and the Gas Čerenkov for π^-s in the HRS_e. A sharp, clear coincidence ToF peak with a FWHM of 1.8 ns and a typical signal-to-noise ratio of 8:1 resulted (see Figure 3). High energy correlated protons which punched through the HRS_h collimator (<10% of the prompt yield) were rejected by requiring both spectrometers to independently reconstruct the coincidence event vertex in the vicinity of the same water film. The resulting prompt peak yields for each water film were corrected for uncorrelated (random) events present in the peak timing region on a bin-by-bin basis [62]. These per-film yields

were then normalized individually.

B. Normalization

The relative focal plane efficiencies for each of the two spectrometers were measured independently for each of the three water films at every spectrometer excitation used in the experiment. By measuring the same single-arm cross section at different positions across the spectrometer focal planes, variations in the relative efficiencies were identified. The position variation across the focal plane was investigated by systematically shifting the central excitation of the spectrometer about the mean momentum setting in a series of discrete steps such that the full momentum acceptance was mapped. A smooth, slowly varying dip-region cross section was used instead of a single discrete peak for continuous coverage of the focal plane. The relative efficiency profiles were unfolded from these data using the program RELEFF [63]. For each water film, solid angle cuts were then applied to select the flat regions of the angular acceptance. These cuts reduced the spectrometer apertures by roughly 20% to about 4.8 msr. Finally, relative momentum cuts were applied to select the flat regions of momentum acceptance. These cuts reduced the spectrometer momentum acceptance by roughly 22% to $-3.7\% < \delta < 3.3\%$. The resulting acceptance profile of each spectrometer was uniform to within 1%.

The absolute efficiency at which the two spectrometers operated in coincidence mode was given by

$$\epsilon = \epsilon_e \cdot \epsilon_p \cdot \epsilon_{\rm coin}, \qquad (1)$$

where ϵ_e was the single-arm HRS$_e$ efficiency, ϵ_p was the single-arm HRS$_h$ efficiency, and $\epsilon_{\rm coin}$ was the coincidence trigger efficiency. The quantity $(\epsilon_p \cdot \epsilon_{\rm coin})$ was measured in parallel kinematics at $E_{\rm beam} = 0.843$ GeV using the ^{1}H(e,e) reaction. A 0.7 msr collimator was placed in front of the HRS$_e$. In these kinematics, the cone of recoil protons fit entirely into the central flat acceptance region of the HRS$_h$. The number of ^{1}H(e,e) events where the proton was detected was compared to the number of ^{1}H(e,e) events where it was not to yield a product of efficiencies $(\epsilon_p \cdot \epsilon_{\rm coin})$ of 98.9%. The 1.1% effect was due to proton absorption in the waterfall target exit windows, spectrometer windows, and the first layer of trigger scintillators. Since the central field of the HRS$_h$ was held constant throughout the entire experiment, this measurement was applicable to each of the hadron kinematics employed. A similar method was used to determine the quantity $(\epsilon_e \cdot \epsilon_{\rm coin})$ at each of the three HRS$_e$ field settings. Instead of a collimator, software cuts applied to the recoil protons were used to ensure the cone of scattered electrons fit entirely into the central flat acceptance region of the HRS$_e$. This product of efficiencies was >99%. Thus, the coincidence efficiency $\epsilon_{\rm coin}$ was firmly established at nearly 100%. A nominal sytematic uncertainty of ±1.5% was attribued to ϵ.

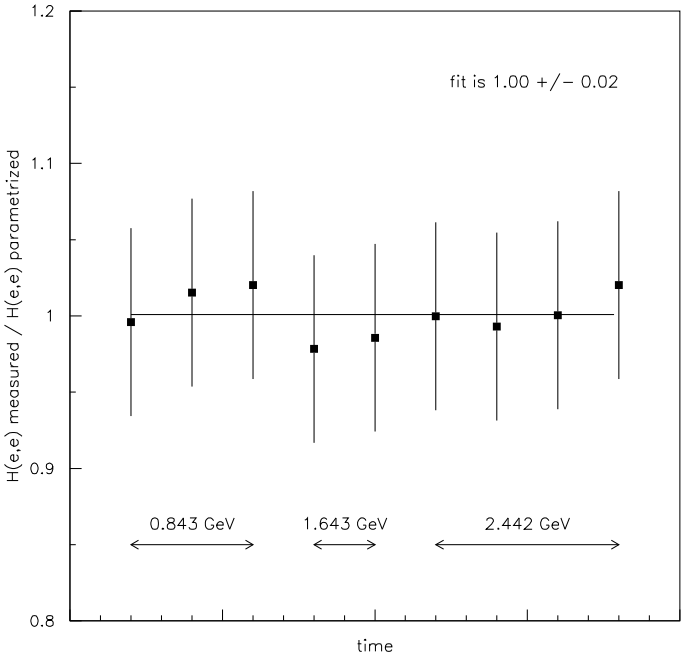

FIG. 4: Measured ^{1}H(e,e) cross sections normalized to the absolute predictions of a parametrization at similiar Q^2 [64, 65]. Statistical error bars are shown. Time flows from left to right and the figure encompasses a three-month run period. The different data points for each $E_{\rm beam}$ represent different HRS$_h$ angular settings.

The quantity $(\ell \cdot \epsilon_e)$, where ℓ is the luminosity (the product of the effective target thickness and the number of incident electrons) was determined to ±4% by comparing the measured ^{1}H(e,e) cross section for each film at each of the electron kinematics to a parametrization established at a similar Q^2 [64, 65] (see Figure 4). The results reported in this paper have all been normalized in this fashion. As a consistency check, direct absolute calculation of $(\ell \cdot \epsilon_e)$ using information from the BCMs, the calibrated thicknesses of the water films, and the single-arm HRS$_e$ efficiency agrees within error.

At every kinematics, a Monte Carlo of the phase space volume subtended by each experimental bin was performed. For each water foil, N_0 software $(e,e'p)$ events were generated, uniformly distributed over the scattered electron and knocked-out proton momenta (p_e, p_p) and in-plane and out-of-plane angles (ϕ_e, θ_e, ϕ_p, θ_p). For each of these events, all of the kinematic quantities were calculated. The flat-acceptance cuts determined in the analysis of the relative focal plane efficiency data were then applied, as were all other cuts that had been performed on the actual data. The pristine detection volume $\Delta V_b(E_{\rm miss}, P_{\rm miss}, \omega, Q^2)$ subtended by a bin $b(\Delta E_{\rm miss}, \Delta P_{\rm miss}, \Delta\omega, \Delta Q^2)$ containing N_b pseudoevents was thus

$$\Delta V_b(E_{\rm miss}, P_{\rm miss}, \omega, Q^2) = \frac{N_b}{N_0}\,[(\Delta p_e \cdot \Delta\Omega_e)\cdot(\Delta p_p \cdot \Delta\Omega_p)], \tag{2}$$

where the quantity $(\Delta p_e \cdot \Delta\Omega_e)\cdot(\Delta p_p \cdot \Delta\Omega_p)$ was the total volume sampled over in the Monte Carlo (purposely set larger than the experimental acceptance in all dimensions) [105]. The pseudodata were binned exactly as the real data, and uniformly on both sides of $\vec{q}$. At each kinematics, the bin with the largest volume $\Delta V_{\rm max}$ was located. Only bins subtending volumes larger than 50% of $\Delta V_{\rm max}$ were analyzed further.

Corrections based on the TS output-to-input ratio were applied to the data to account for the acquisition deadtime to coincidence events. On average, these corrections were roughly 20%. An acquisition Monte Carlo [66] was used to cross-check these corrections and establish the absolute uncertainty in them at 2%.

Corrections to the per-film cross sections for electron radiation before and after scattering were calculated using both a modified version of the code RADCOR [67, 68] and independently, the prescriptions of Borie and Dreschel [69] contained within the simulation package MCEEP [70, 71] on a bin-by-bin basis. The two approaches agreed to within the statistical uncertainty of the data and amounted to <55% (<15%) of the measured cross section for the bound states (continuum). Corrections for proton radiation at these energies are much less than 1% and were not performed.

C. Cross sections

The radiatively corrected average cross section in the bin $b(\Delta E_{\rm miss},\, \Delta P_{\rm miss},\, \Delta\omega,\, \Delta Q^2)$ was calculated according to

$$\left\langle \frac{d^6\sigma}{d\omega\; d\Omega_e\; dE_{\rm miss}\; d\Omega_p} \right\rangle_b = \frac{R_{^{16}{\rm O}(e,e'p)}}{(\ell\cdot\epsilon_e)(\epsilon_p\cdot\epsilon_{\rm coin})} \left(\frac{Y_b}{\Delta V_b}\right), \tag{3}$$

where Y_b was the total number of real events which were detected in $b(\Delta E_{\rm miss},\, \Delta P_{\rm miss},\, \Delta\omega,\, \Delta Q^2)$, $(\ell\cdot\epsilon_e)$ was determined from the ratio of the measured $^1{\rm H}(e,e)$ cross section to the parametrized cross section, $(\epsilon_p\cdot\epsilon_{\rm coin})$ was the product of the proton and coincidence detection efficiency, ΔV_b was the phase space volume, and $R_{^{16}{\rm O}(e,e'p)}$ was a correction applied to account for events which radiated out of ΔV_b. The average cross section was calculated as a function of $E_{\rm miss}$ for a given kinematic setting [106]. Bound-state cross sections for the $1p$-shell were extracted by integrating over the appropriate range in $E_{\rm miss}$, weighting with the appropriate Jacobian [107]. Five-fold differential cross sections for quasielastic proton knockout from the $1p$-shell of ^{16}O are presented in Tables VIII and IX. Six-fold differential cross sections for quasielastic proton knockout from ^{16}O at higher missing energies are presented in Tables X through XIX.

D. Asymmetries and response functions

In the first Born (one-photon exchange) approximation, the unpolarized six-fold differential cross section may be expressed in terms of four independent response functions as [6, 72, 73]

$$\frac{d^6\sigma}{d\omega\; d\Omega_e\; dE_{\rm miss}\; d\Omega_p} = K\;\sigma_{\rm Mott}\left[v_L R_L + v_T R_T + v_{LT} R_{LT}\cos(\phi) + v_{TT} R_{TT}\cos(2\phi)\right], \tag{4}$$

where K is a kinematic factor, $\sigma_{\rm Mott}$ is the Mott cross section, and the $v_{\rm i}$ are dimensionless kinematic factors [108]. Note that the $v_{\rm i}$ depend only on $(\omega,\, Q^2)$, while the response functions depend on $(\omega,\, Q^2,\, E_{\rm miss},\, P_{\rm miss})$. The response functions are denoted R_L (longitudinal), R_T (transverse), R_{LT} (longitudinal-transverse), and R_{TT} (transverse-transverse). They contain all the information which may be extracted from the hadronic system using $(e,e'p)$.

The individual contributions of the response functions may be separated by performing a series of cross section measurements varying $v_{\rm i}$ and/or ϕ, but keeping $\vec{q}$ and ω constant [109]. In the case where the proton is knocked-out of the nucleus in a direction parallel to $\vec{q}$ (parallel kinematics), the interference terms R_{LT} and R_{TT} vanish, and a Rosenbluth separation [74] may be performed to separate R_L and R_T. In the case where the proton is knocked-out of the nucleus in the scattering plane with a finite angle θ_{pq} with respect to $\vec{q}$ (quasi-perpendicular kinematics), the asymmetry A_{LT} and the interference R_{LT} may be separated by performing symmetric cross section measurements on either side of $\vec{q}$. The contribution of R_{TT} cannot be separated from that of R_L with only in-plane measurements; however, by combining the two techniques, an interesting combination of response functions R_{L+TT} [110] may be extracted.

For these data, response function separations were performed where the phase space overlap between kinemat-

TABLE III: Kinematic-dependent systematic uncertainties folded into the MCEEP simulation suite.

Quantity	description	δ
$E_{\rm beam}$	beam energy	1.6×10^{-3}
$\phi_{\rm beam}$	in-plane beam angle	ignored[a]
$\theta_{\rm beam}$	out-of-plane beam angle	2.0 mr
p_e	scattered electron momentum	1.5×10^{-3}
ϕ_e	in-plane scattered electron angle	0.3 mr
θ_e	out-of-plane scattered electron angle	2.0 mr
p_p	proton momentum	1.5×10^{-3}
ϕ_p	in-plane proton angle	0.3 mr
θ_p	out-of-plane proton angle	2.0 mr

[a]The angle of incidence of the electron beam was determined using a pair of beam position monitors (BPMs) [38, 39] located upstream of the target (see Figure 2). The BPM readback was calibrated by comparing the location of survey fiducials along the beamline to the Hall A survey fiducials. Thus, in principle, uncertainty in the knowledge of the incident electron beam angle should be included in this analysis. However, the simultaneous measurement of the overdetermined ^{1}H(e,ep) reaction allowed for a calibration of the absolute kinematics, and thus an elimination of this uncertainty. That is, the direction of the beam defined the axis relative to which all angles were measured via ^{1}H(e,ep).

ics permitted. For these separations, bins were selected only if their phase space volumes ΔV_b were all simultaneously 50% of $\Delta V_{\rm max}$. Separated response functions for quasielastic proton knockout from the $1p$-shell ^{16}O are presented in Tables XX, XXI, and XXII. Separated response functions for quasielastic proton knockout from the ^{16}O continuum are presented in Tables NILANGA3, NILANGA4, and NILANGA5.

E. Systematic uncertainties

The systematic uncertainties in the cross section measurements were classified into two categories - kinematic-dependent uncertainies and scale uncertainties. For a complete discussion of how these uncertainties were evaluated, the interested reader is directed to [75]. For the sake of completeness, a subset of the aforementioned information is presented here.

In a series of simulations performed after the experiment, MCEEP [71] was used to investigate the intrinsic behavior of the cross section data when constituent kinematic parameters were varied over the appropriate experimentally determined ranges presented in Table III. Based on the experimental data, we modelled the high-$E_{\rm miss}$ region as the superposition of a peak-like $1s_{1/2}$-state on a flat continuum. Contributions to the systematic uncertainty from this flat continuum were taken to be small, leaving only those from the $1s_{1/2}$-state. The ^{16}O$(e,e'p)$ simulations incorporated the latest bound-state calculations of Udías *et al.* [19] as physics input, which were based on the experimental $1p$-shell data.

For each kinematics, the central water foil was considered, and 1M events were generated. In evaluating the simulation results, the exact cuts applied in the actual data analyses were applied to the pseudo-data, and the cross sections were evaluated for the identical $P_{\rm miss}$ bins used to present the results. The experimental constraints to the kinematic-dependent observables afforded by the overdetermined ^{1}H(e,ep) reaction were exploited to calibrate or constrain the experimental setup. The in-plane electron and proton angles ϕ_e and ϕ_p were chosen as independent parameters. When a known shift in ϕ_e was made, ϕ_p was held constant and the complementary variables $E_{\rm beam}$, p_e, and p_p were varied as required by the constraints enforced by the ^{1}H(e,ep) reaction. Similarly, when a known shift in ϕ_p was made, ϕ_e was held constant and the complementary variables $E_{\rm beam}$, p_e, and p_p were varied as appropriate. The overall constrained uncertainty was taken to be the quadratic sum of the two contributions.

The global convergence of the uncertainty estimate was examined for certain extreme kinematics, where 10M-event simulations (which demonstrated the same behavior) were performed. The behavior of the uncertainty as a function of $P_{\rm miss}$ was also investigated by examining the uncertainty in the momentum bins adjacent to the reported momentum bin in exactly the same fashion.

The kinematically induced systematic uncertainty in the ^{16}O$(e,e'p)$ cross sections was determined to be dependent upon $P_{\rm miss}$, with an average value of 1.4%. The corresponding uncertainties in the ^{1}H(e,e) cross sections were determined to be negligible.

The scale systematic uncertainties which affect each of the cross section measurements are presented in Table IV. As previously mentioned, the ^{16}O$(e,e'p)$ cross section results reported in this paper have been normalized by comparing simultaneously measured ^{1}H(e,e) cross sections to a parametrization established at a similar Q^2 [64, 65]. Thus, the first seven listed uncertainties simply divide out of the quotient, such that only the last five uncertainties affect our results. The quadratic sum of these last five entries is 5.4%. The average systematic uncertainty associated with a $1p$-shell (continuum) cross section was 5.6% (5.9%). The small difference was due to contamination of the high-$E_{\rm miss}$ data by collimator punch-through events.

The quality of these data in terms of their associated systematic uncertainties was clearly demonstrated by the results obtained for the structure function separations. For example, in Figure 5, cross sections measured in parallel kinematics at three different beam energies as a function of the separation lever arm for the $1p$-shell are shown. The values of the response functions R_L (offset) and R_T (slope) were extracted from the fitted line. The extremely linear trend in the data indicated that the magnitude of the systematic uncertainties was small, and statistical uncertainties dominated.

The systematic quality of the data was also demonstrated by the results extracted from identical measurements which were performed in different electron kinematics. The asymmetries A_{LT} and response functions

TABLE IV: Summary of the scale systematic uncertainties contributing to the cross section measurements. The first seven entries do not contribute to the systematic uncertainties in the reported cross sections as they contribute equally to the ^{1}H(e,e) cross sections to which the ^{16}O$(e,e'p)$ are normalized.

Quantity	description	δ (%)
$\eta_{\rm DAQ}$	data acquisition deadtime correction	2.0
$\eta_{\rm elec}$	electronics deadtime correction	<1.0
$\rho t'$	effective target thickness	2.5
N_e	number of incident electrons	2.0
ϵ_e	electron dectection efficiency	1.0
$\Delta\Omega_e$ [a]	HRS$_e$ solid angle	2.0
$\epsilon_e\epsilon_p\epsilon_{\rm coin}$	product of electron, proton, and coincidence efficiencies	1.5
$\ell\cdot\epsilon_e$	obtained from a form factor parametrization of ^{1}H(e,e)	4.0
$R_{^{16}{\rm O}(e,e'p)}$ [b]	radiative correction to the ^{16}O$(e,e'p)$ data	2.0
$R_{^1{\rm H}(e,e)}$ [b]	radiative correction to the ^{1}H(e,e) data	2.0
$\epsilon_p\epsilon_{\rm coin}$	product of proton and coincidence efficiencies	<1.0
$\Delta\Omega_p$ [a]	HRS$_h$ solid angle	2.0
punchthrough [c]	protons which punched through the HRS$_h$ collimator	2.0

[a] The systematic uncertainties in the solid angles $\Delta\Omega_e$ and $\Delta\Omega_p$ were quantified by studying sieve-slit collimator optics data at each of the spectrometer central momenta employed. The angular locations of each of the reconstructed peaks corresponding to the 7×7 lattice of holes in the sieve slit plate were compared to the locations predicted by spectrometer surveys, and the overall uncertainy was taken to be the quadratic sum of the individual uncertainties.

[b] At first glance, it may be surprising to note that the uncertainty due to the radiative correction to the data is included as a scale uncertainty. In general, the radiative correction is strongly dependent on kinematics. However, the $1p$-shell data analysis, and for that matter any bound-state data analysis, involves missing energy cuts. These cuts to a large extent remove the strong kinematic dependence of the radiative correction, since only relatively small photon energies are involved. In order to compensate for any remaining weak kinematic dependence, the uncertainty due to the radiative correction was slightly overestimated.

[c] High $E_{\rm miss}$ data only.

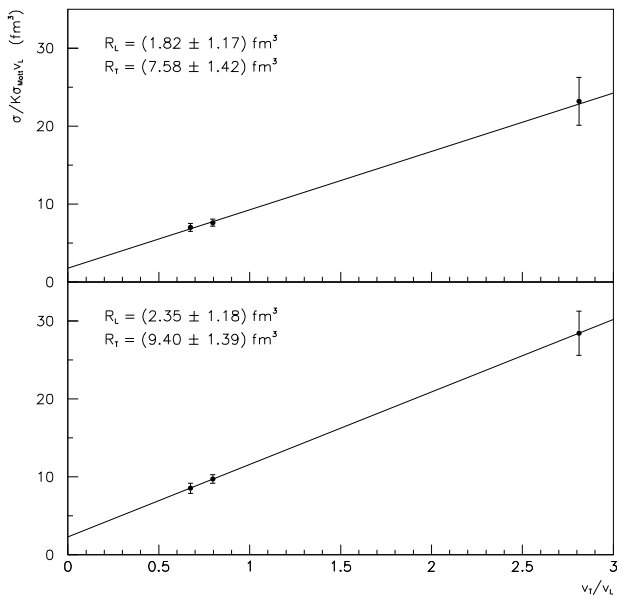

FIG. 5: Cross sections measured in parallel kinematics at three different beam energies as a function of the separation lever arm for the $1p$-shell. The data points correspond to beam energies of 2.442, 1.643, and 0.843 GeV from left to right. The response functions R_L (offset) and R_T (slope) have been extracted from the fitted line. Uncertainties are statistical only. The extremely linear behavior of the data indicates the systematic uncertainties were dominated by statistical uncertainties.

R_{LT} for quasielastic proton knockout from the $1p$-shell of ^{16}O for $<Q^2>=0.800$ (GeV/c)^2, $<\omega>=436$ MeV, and $<T_p>=427$ MeV for both the $E_{\rm beam}=1.643$ GeV and 2.442 GeV data are presented in Table XXII. The excellent agreement of these values again indicates that the systematic uncertainties were much smaller than the statistical uncertainties. Further, in Figure 6, R_{LT} measured for $\theta_{pq}=\pm8^\circ$ ($P_{\rm miss}\approx148$ MeV/c) as a function of $E_{\rm miss}$ is shown for $E_{\rm beam}=1.643$ GeV and 2.442 GeV. The extracted response functions all agree within statistics.

IV. DISCUSSION

The data were interpreted in subsets corresponding to the $1p$-shell and continuum, respectively. The interested reader is directed to [76, 77], where these results have been highlighted.

1. $1p$-shell results

The consistency of the spectroscopic factors suggested by the $1p$-shell data obtained from this measurement with respect to those suggested by the other ^{16}O$(e,e'p)$ data sets known to the authors (see Table V) was examined by Kelly [78].

The data were all examined using the same type of calculation - a solution to a relativized Schrödinger equation

TABLE V: Summary of the kinematic conditions for the data sets surveyed by Kelly [78].

label	authors	kinematics	T_p (MeV)	Q^2 $(\mathrm{GeV}/c)^2$	x	$2s_{1/2}1d_{5/2}$-doublet	data
a	Leuschner *et al.* [12]	parallel	96	varied	varied	resolved	reduced σ
b	Spaltro *et al.* [11]	perpendicular	84	0.20	1.07	resolved	reduced σ
c	Chinitz *et al.* [10]	perpendicular	160	0.30	0.91	computed [a]	differential σ
d	this work	perpendicular	427	0.80	0.96	computed [b]	differential σ
e	Bernheim *et al.* [9]	perpendicular	100	0.19	0.90	computed [b]	reduced σ
f	Blomqvist1 *et al.* [13]	parallel	92	0.08	0.30 - 0.50	resolved	reduced σ
g	Blomqvist2 *et al.* [13]	highly varied	215	0.04 - 0.26	0.07 - 0.70	resolved	reduced σ

[a] The $1p_{3/2}$-state data were corrected for the doublet contamination by the authors.
[b] The $1p_{3/2}$-state doublet contamination was computed by incoherently including the parametrizations of [12].

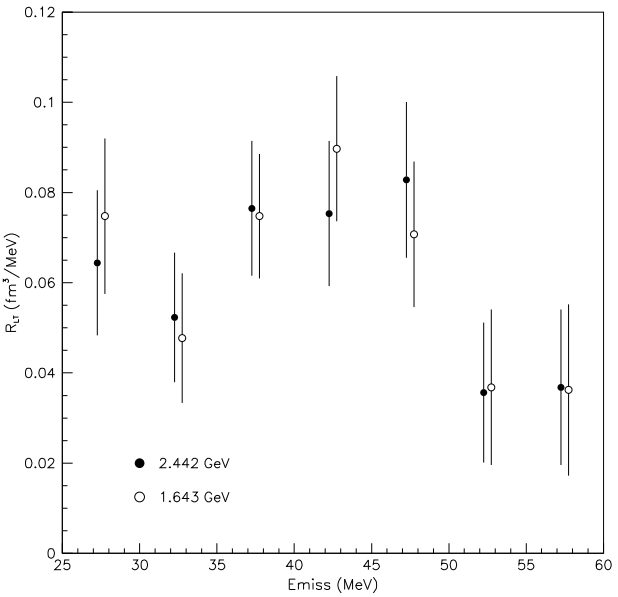

FIG. 6: R_{LT} measured for $\theta_{pq} = \pm 8^\circ$ ($P_{\mathrm{miss}} \approx 148$ MeV/c) as a function of E_{miss} for $E_{\mathrm{beam}} = 1.643$ GeV and 2.442 GeV. Statistical uncertainties only are shown. This statistical agreement over a broad range of E_{miss} emphasizes the systematic precision of the measurement. See also Table NILANGA.

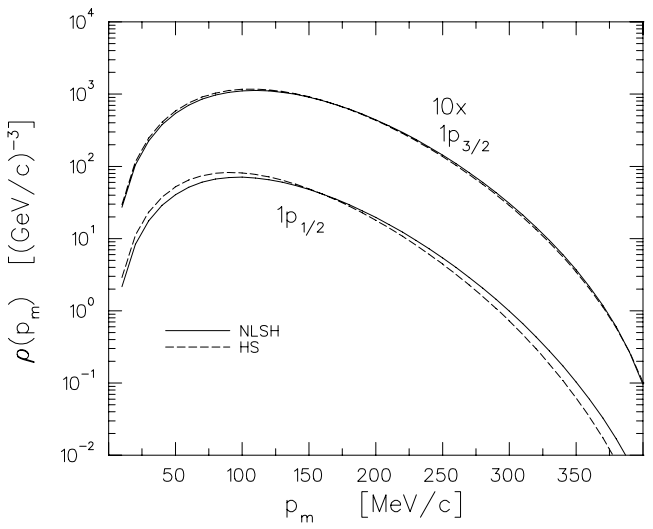

FIG. 7: PWIA momentum distributions for the NLSH [83] and HS [84] models. Appreciable difference exists for the $1p_{3/2}$-state distributions, but there is little to distinguish between the $1p_{1/2}$-state distributions. Note that the NLSH wave function predicts binding energies, single-particle energies, and a charge radius for ^{16}O which are all in good agreement with the data.

which employed the Effective Momentum Approximation (EMA) [2, 79] to build spinor distortion in to an effective current operator based on that of Hedayati-Poor *et al.* [80]. The calculation employed the Coulomb gauge [REF] and the CC2 current operator [81], the MMD [82] nucleon form factor model, and included the effects of electron distortion. The bound-nucleon wave function was varied between the NLSH [83] and HS [84] models (see Figure 7). Note that the NLSH wave function predicts binding energies, single-particle energies, and a charge radius for ^{16}O which are all in good agreement with the data. The optical potential was varied between two purely phenomenological SV potentials developed by Cooper *et al.* [85] and based upon the Dirac equation: EDAI-O (an energy-dependent, atomic-mass independent parametrization for ^{16}O) and EDAD1 (an energy-dependent, atomic-mass dependent parametrization). The resulting curves were fitted to the cross section data. The spectroscopic factors S_α were the result of this fit, effectively normalizing the calculation to the data. The results of this study are presented in Table VI.

Qualitatively, the HS bound-nucleon wave function fitted the low Q^2 data better (particularly for the Leuschner *et al.* experiment), while the NLSH bound-nucleon wave function fitted the data from this work better. Further, within this framework, the data sets demonstrated a slight preference for the EDAD1 optical potential over the EDAI-O optical potential. This was concluded based on the quality of the fits and the more consistent nature of the extracted spectroscopic factors. As previously mentioned, data set (g) from Blomqvist *et al.* suggested a

TABLE VI: Spectroscopic factors deduced by Kelly [78] for the data sets presented in Table V. The first term in brackets is for the $1p_{1/2}$-state, while the second term in brackets is for the $1p_{3/2}$-state.

label	authors	NLSH / EDAI-O	NLSH / EDAD1	HS / EDAI-O	S_α HS / EDAD1
a	Leuschner *et al.* [12]	(0.62,0.53)	(0.69,0.61)	(0.55,0.50)	(0.60,0.58)
b	Spaltro *et al.* [11]	(0.70,0.70)	(0.82,0.80)	(0.63,0.67)	(0.72,0.75)
c	Chinitz *et al.* [10]	(0.65,0.60)	(0.70,0.65)	(0.55,0.55)	(0.60,0.63)
d	this work	(0.71,0.65)	(0.71,0.65)	(0.61,0.62)	(0.61,0.62)
e	Bernheim *et al.* [9]	(0.55,0.52)	(0.55,0.55)	(0.50,0.50)	(0.50,0.53)
f	Blomqvist1 *et al.* [13]	(0.55,0.42)	(0.60,0.50)	(0.52,0.42)	(0.55,0.52)
g	Blomqvist2 *et al.* [13]	(0.47,0.38)	(0.48,0.42)	(0.42,0.36)	(0.42,0.40)

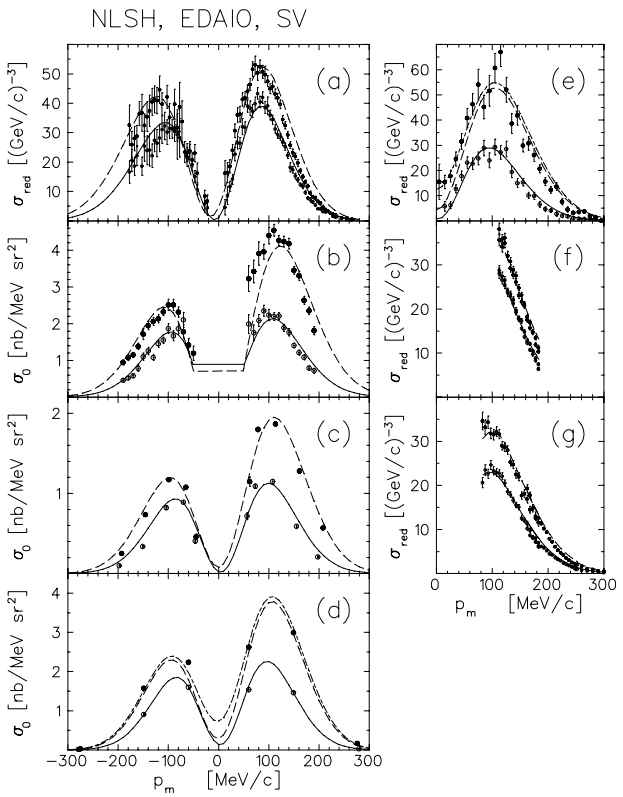

FIG. 8: Fits by Kelly [78] to various ^{16}O$(e,e'p)$ data sets based on the NLSH [83] bound-nucleon wave function and the EDAI-O [85] optical potential. See text for details. Open points and solid lines pertain to the $1p_{1/2}$-state, while solid points and dashed lines pertain to the $1p_{3/2}$-state. The dashed-dotted lines include the contributions of the $2s_{1/2}1d_{5/2}$-doublet to the $1p_{3/2}$-state. See Table V or VI for the key to the data sets. (b) SHOULD BE $\sigma_{\rm red}$ I THINK.

substantially different normalization.

Udías *et al.* [86] also performed a spectroscopic study, focusing on the 2.442 GeV $1p$-shell data obtained in this work (see Table IX). In each set of calculations, the input was varied over a wide range of basis options (approach, current operator, bound-nucleon wave function, optical potential, gauge, nucleon form factor model, and doublet contribution) and the resulting curves were then fitted to the cross section data. The projected spectroscopic factor S_α was the result of this fit, again effectively normalizing the calculations to the data.

Three basic approaches were considered: fully relativistic [111] and projected [17, 18], and EMA-noSV [2, 79]. All approaches included the effects of electron distortion. The fully relativistic approach involved solving the Dirac equation directly in configuration space. The projected approach included only the positive energy components, and as a result, most (but not all) of the spinor distortion was removed from the wave functions. Within the EMA-noSV approach, a relativized Schrödinger equation was solved using the EMA, and all of the spinor distortion was removed. This made the calculation more-or-less identical to a factorized calculation. The current operator was varied between CC1 and CC2. Three bound-nucleon wave functions derived from relativistic Langrangians were also considered: NLSH, NLSH-P [87], and HS. Recall that NLSH yielded values of the binding energy, single-particle energies, and charge radius for ^{16}O which are in good agreement with data. The NLSH-P wave function resulted from a Langrangian fine-tuned to reproduce the low $P_{\rm miss}$ data of Leuschner *et al.*. Differences due to choice of either the Coulomb, Weyl, and Landau gauge prescriptions [REF] were investigated. Because of the large number of optical potentials available at $T_p \approx 400$ MeV, five were investigated. These potentials included the previously discussed EDAI-O and EDAD1, a slightly modified energy-dependent, atomic-mass dependent parametrization by Cooper *et al.* called EDAD2 [85], as well as MRW [88] and RLF [89, 90]. [WORDS ABOUT MRW AND RLF.] Two different nucleon form factor models (GK [91] and the dipole model [REF]) were considered. Effects due to the density dependence of the GK form factors were investigated by building in a density dependence similar to that derived for the QMC [92, 93] form factors. And finally, the effect of different mixing ratios for the $2s_{1/2}1d_{5/2}$-doublet and the $1p_{3/2}$-state were considered. The nominal strength of this doublet was taken to be 5% of the stregth of the $1p_{3/2}$-state using the spectroscopic factors of Leuschner *et al.*. The results of these calculations are presented in Table VII.

Qualitatively, the fully relativistic approach clearly did

TABLE VII: Spectroscopic factors derived by Udías *et al.* [86] from the 2.442 GeV 1p-shell cross section data of Table IX using the CC1 and CC2 [81] current operators. The numbers within parentheses indicate the associated statistical error in %. See text for details.

state	prescription			bound-nucleon wavefunction			gauge			optical Potential					nucleon form factor model			doublet-%			S_α		χ^2/dof	
	fully relativistic	projected	EMA noSV	NLSH	NLSH-P	HS	Coulomb	Weyl	Landau	EDAI-0	EDAD1	EDAD2	MRW	RLF	GK	dipole	QMC	100	50	0	CC1	CC2	CC1	CC2
$1p_{1/2}$	X			X			X			X					X			X			0.68(4)	0.74(3)	5.5	2.0
		X		X			X			X					X			X			0.78(8)	0.76(5)	17.0	8.0
			X	X			X			X					X			X			0.72(3)	0.75(3)	2.3	2.2
	X				X		X			X					X			X			0.60(5)	0.63(6)	10.0	15.0
	X					X	X			X					X			X			0.62(5)	0.65(7)	10.0	18.0
	X			X				X		X					X			X			0.63(8)	0.76(3)	25.0	2.6
	X			X					X	X					X			X			0.69(3)	0.73(3)	3.7	2.5
	X			X			X				X				X			X			0.64(8)	0.72(4)	29.0	4.8
	X			X			X					X			X			X			0.64(6)	0.71(1)	15.0	0.7
	X			X			X						X		X			X			0.62(9)	0.71(5)	35.0	7.6
	X			X			X							X	X			X			0.61(10)	0.70(4)	41.0	6.1
	X			X			X			X						X		X			0.69(4)	0.75(3)	4.8	2.1
	X			X			X			X							X	X			0.65(5)	0.72(1)	11.0	0.5
$1p_{3/2}$	X			X			X			X					X			X			0.62(3)	0.67(8)	5.3	31.0
		X		X			X			X					X			X			0.73(13)	0.71(12)	79.0	70.0
			X	X			X			X					X			X			0.66(11)	0.69(11)	65.0	65.0
	X				X		X			X					X			X			0.52(10)	0.54(12)	97.0	115.0
	X					X	X			X					X			X			0.61(3)	0.65(8)	6.7	41.0
	X			X				X		X					X			X			0.59(4)	0.70(7)	9.2	22.0
	X			X					X	X					X			X			0.63(3)	0.67(8)	6.4	34.0
	X			X			X				X				X			X			0.60(4)	0.67(4)	12.0	8.2
	X			X			X					X			X			X			0.59(3)	0.65(5)	6.4	15.0
	X			X			X						X		X			X			0.60(4)	0.67(4)	11.0	7.3
	X			X			X							X	X			X			0.58(4)	0.65(4)	12.0	7.9
	X			X			X			X						X		X			0.63(3)	0.68(8)	5.9	31.0
	X			X			X			X							X	X			0.61(2)	0.66(5)	3.3	16.0
	X			X			X			X					X				X		0.64(3)	0.70(8)	6.1	33.0
	X			X			X			X					X					X	0.66(3)	0.72(8)	7.4	35.0

the best job of reproducing the data. CC2 was in general less sensitive to changes in the bound-nucleon wave function. The choice of wave function primarily affected the $P_{\rm miss}$-location of the ripple in A_{LT}. Fully relativistic results were shown to be much less gauge-dependent than the non-relativistic results. The CC2 current operator was also in general less sensitive to choice of gauge. The data discouraged the choice of the Weyl gauge. The different optical models had little effect on the shape of the calculations, but instead determined the magnitude. Both the GK and dipole models produced nearly identical results. The change in the calculated GK+QMC cross section was modest, being most pronounced in A_{LT} for $P_{\rm miss} > 300$ MeV/c. And finally, the results were best for a 100% contribution of the strength of the $2s_{1/2}1d_{5/2}$-doublet to the $1p_{3/2}$-state, although the data were not terribly sensitive to this degree-of-freedom. The ingredients to the baseline calculation of Udías *et al.* were thus determined. This fully relativistic calculation employed the CC2 current operator, used NLSH for the bound-nucleon wave function, and the EDAI-O optical potential for FSI. The Coulomb gauge was selected, and the GK nucleon form factor model was employed. Finally, a full contribution of the $2s_{1/2}1d_{5/2}$-doublet (determined using the spectroscopic factors of Leuschner *et al.*) relative to the $1p_{3/2}$-state was made.

Figure 9 shows the measured cross sections for the $1p$-shell compared to relativistic DWIA calculations for $E_{\rm beam} = 2.442$ GeV. The error bars are statisical, and on average, an additional $\pm 5.6\%$ systematic uncertainty should be associated with the data points (see Table IX). The $1p_{1/2}$-state cross sections and calculations shown in the top panel have been scaled by a factor of 20. The solid line is the baseline calculation of Udías *et al.*, while the dashed line is a relativistic calculation from Kelly [94]. Note that this calculation is not the same as that shown in our previous Letter [76], and its ingredients and framework are now essentially identical [112] to those used in the Udías *et al.* calculation. The $1p_{1/2}$-state ($1p_{3/2}$-state) spectroscopic factors are 0.73 (0.72) for the calculations of Udías *et al.*, and 0.80 (0.70) for the calculation of Kelly. The bottom panel demonstrates the excellent agreement between the data and the calculation of Udías *et al.* over a wide range of $P_{\rm miss}$ and on a linear scale. This agreement is due to the quality of the NLSH bound-nucleon wave function employed in the calculation.

Figure 10 shows the left-right asymmetry A_{LT} for the $1p$-shell compared to the previously detailed relativistic DWIA calculations for $E_{\rm beam} = 2.442$ GeV. The error bars are again statistical, and on average, an additional $\pm$X.X% ($\pm$X.X%) systematic uncertainty should be associated with the $1p_{1/2}$ ($1p_{3/2}$) data points (see Table XXII). Note the large change in the slope of A_{LT} at $P_{\rm miss} \approx 300$ MeV/c. The solid curve is the fully relativistic baseline calculation of of Udías *et al.*, which nicely reproduces this change in slope. In his nearly identical calculation (the dashed curve in Figure 10), Kelly sees the exact

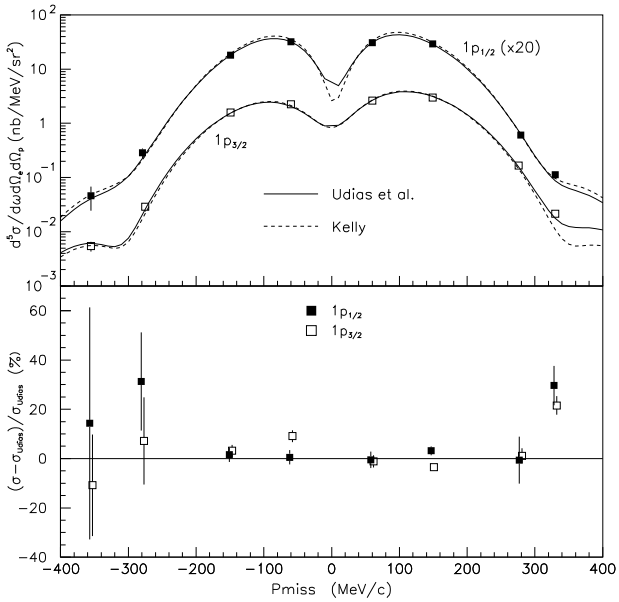

FIG. 9: $P_{\rm miss}$-dependence of the measured cross sections for the $1p$-shell as compared to relativistic DWIA calculations for $E_{\rm beam} = 2.442$ GeV. For better readability, the $1p_{1/2}$-state cross sections and calculations shown in the top panel have been scaled by a factor of 20. Error bars are statistical and on average, an additional $\pm 5.6\%$ systematic uncertainty should be associated with the data points (see Table IX). The solid line is the relativistic calculation taken from Udías *et al.* [17, 19], while the dashed line comes from Kelly [94]. Note that the calculation of Kelly shown here is relativistic and not the same as that shown in our previous Letter [76] (see text for details). The input to the two calculations as well as the style of the calculations are essentially identical. The bottom panel emphasizes the excellent agreement between the data and the calculation of Udías *et al.* over the entire $P_{\rm miss}$ range. WARNING: KELLY CALCS ARE EYEBALLED.

same effect, which is reassuring. The effect is due to the distortion of the bound-nucleon and ejectile spinors, as evidenced by the other three curves shown, in which the full Udías *et al.* calculation has been decomposed. Note that these three curves all maintain the same basic ingredients, particularly the fully relativistic current operator and the upper components of the Dirac spinors. Of the three curves, the densely dotted line resulted from a calculation where only the bound-nucleon spinor distortion was included, the sparsely dotted line resulted from a calculation where only the scattered-state spinor distortion was included, and the dotted-dashed line resulted from a calculation where undistorted spinors (essentially identical to a factorized calculation) were considered. Clearly, the inclusion of the bound-nucleon spinor distortion is more important than the inclusion of the scattered-state spinor distortion, but both are necessary to describe the data.

The importance of the choice of bound-nucleon wave function and optical potential is illustrated in Figure 11. Here, the $P_{\rm miss}$-dependence of the the left-right

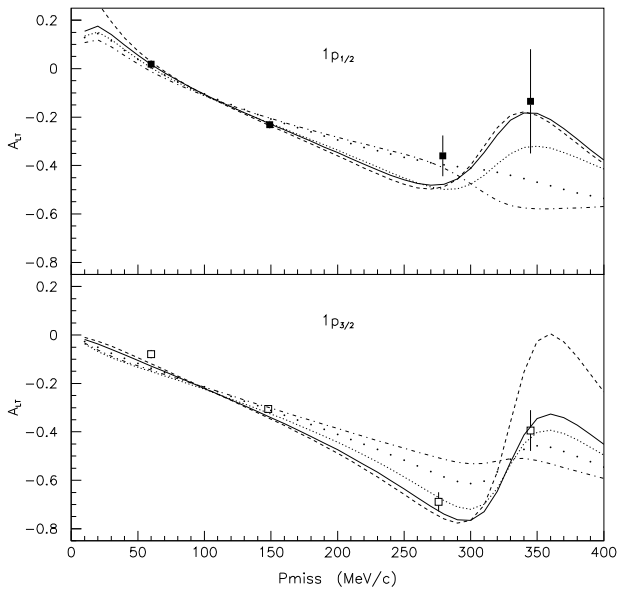

FIG. 10: $P_{\rm miss}$-dependence of the measured A_{LT} asymmetry for the $1p$-shell as compared to relativistic DWIA calculations for $E_{\rm beam} = 2.442$ GeV. Error bars are statistical, and on average, an additional ±X.X% (±X.X%) systematic uncertainty should be associated with the $1p_{1/2}$ ($1p_{3/2}$) data points (see Table XXII). The dashed line is the relativistic calculation from Kelly [94], while the other relativistic curves are from Udías *et al.* [17, 19]. Note that the calculation of Kelly shown here is relativistic and not the same as that shown in our previous Letter [76] (see text for details). The Kelly calculation and the baseline Udías *et al.* calculation (solid line) are essentially identical in both input and method. The densely dotted line is the calculation with only the bound-nucleon spinor distortion included. The sparsely dotted line is the calculation with only the scattered-state spinor distortion included. The dotted-dashed line has no spinor distortion included. WARNING: KELLY CALCS ARE EYEBALLED.

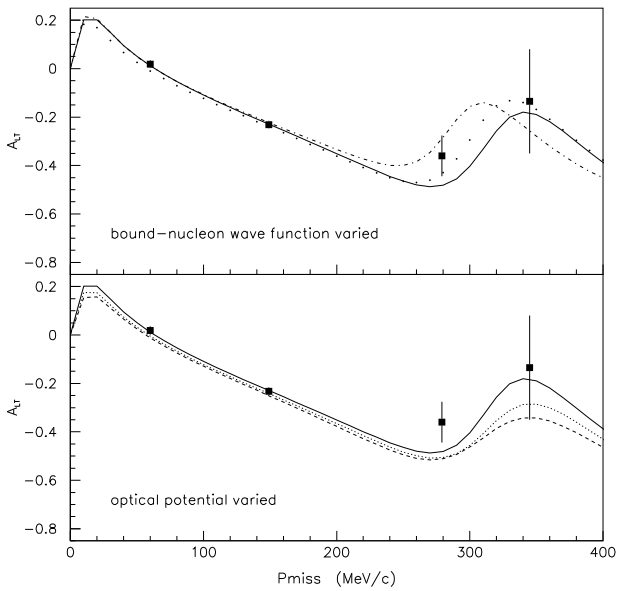

FIG. 11: $P_{\rm miss}$-dependence of the measured A_{LT} asymmetry for the $1p_{1/2}$-state as compared to relativistic DWIA calculations [19] with different bound-state wave functions and optical potentials for $E_{\rm beam} = 2.442$ GeV. Error bars are statistical, and on average, an additional ±X.X% (±X.X%) systematic uncertainty should be associated with the data points (see Table XXII). The solid lines in both panels are the same and represent the baseline calculation of Udías *et al.* [17, 18]. By varying the bound-state wave function employed in the calculation, the $P_{\rm miss}$-location of the ripple may be varied, but the magnitude remains relatively constant. By varying the optical potential, the height of the ripple may be varied, but the $P_{\rm miss}$-location remains constant. See text for details.

asymmetry A_{LT} for the $1p_{1/2}$-state for $E_{\rm beam} = 2.442$ GeV is compared to relativistic DWIA calculations whose bound-nucleon wave functions (top panel) and optical potentials (bottom panel) have been varied. The solid curves in both panels are the same and represent the baseline calculation of Udías *et al.*. For the three curves in the top panel, the EDAI-O optical potential was used. The dot-dashed curve represents the calculation using the NLSH-P bound-nucleon wave function, and the sparsely dotted line represents that using the HS bound-nucleon wave function. As can be clearly seen, the choice of the bound-nucleon wave function controls the $P_{\rm miss}$-location of the ripple but does not affect the magnitude. For the three curves in the bottom panel, the NLSH bound-nucleon wave function was used. The dashed and dotted curves represent the calculation using the EDAD-1 and EDAD-2 optical potentials, respectively. Here, the choice of the optical potential affects the magnitude of the ripple, but the $P_{\rm miss}$-location remains constant.

The R_{L+TT}, R_{LT}, and R_T response functions compared to the previously detailed relativistic DWIA calculations are presented in Figure 12. Note that the data point located at $P_{\rm miss} \approx 52$ MeV/c comes from the parallel kinematics measurements (see Table XX), while the other data points come from the perpendicular kinematics measurements (see Tables XXII and XXI). Strictly, the longitudinal response function R_L could not be separated from the perpendicular kinematics data. However, since both Kelly and Udías *et al.* calculate the term $\frac{v_{TT}}{v_L} R_{TT}$ to be $< 10\%$ of R_{L+TT} in these kinematics, R_L and R_{L+TT} responses are both presented on the same plot. The agreement between calculation and data is good. The spinor distortions which were required to predict the change in slope of A_{LT} at $P_{\rm miss} \approx 300$ MeV/c in Figure 10 are also essential to the description of R_{LT}.

Qualitatively, it should be noted that neither the Kelly nor the Udías *et al.* calculations include contributions from two-body currents. The good agreement between both calculations and the data indicates that these currents are already negligible at $Q^2 = 0.8$ (GeV/c)^2. This observation is supported by independent calculations [95, 96] which estimate the importance of such currents to be large at lower Q^2, but only 2% (8%) for the $1p_{1/2}$-($1p_{3/2}$-) state in these kinematics.

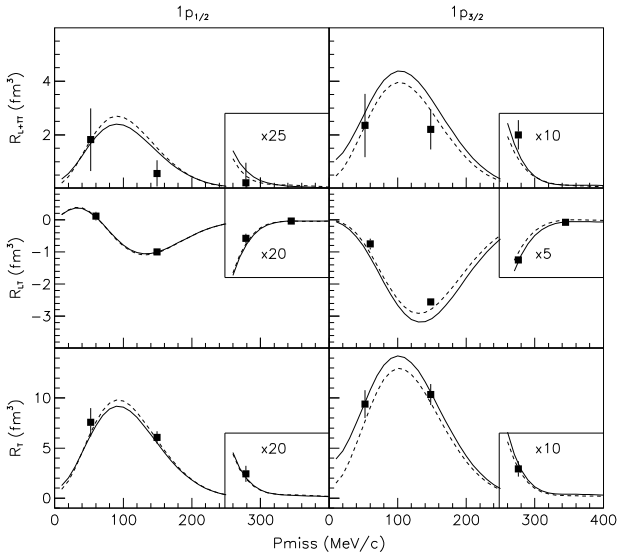

FIG. 12: $P_{\rm miss}$-dependence of the measured R_{L+TT}, R_{LT}, and R_T response functions for the $1p$-shell as compared to relativistic DWIA calculations. Error bars are statistical and on average, an additional ±X.X% (±X.X%) systematic uncertainty should be associated with the $1p_{1/2}$ ($1p_{3/2}$) data points (see Tables XXII, XX, and XXI). The solid line is the relativistic calculation taken from Udías *et al.* [17, 19], while the dashed line is the relativistic calculation from Kelly [94]. Note that the calculation of Kelly shown here is relativistic and not the same as that shown in our previous Letter [76] (see text for details). The data beyond $P_{\rm miss} \approx 250$ MeV/c have been expanded for clarity. WARNING: KELLY CALCS ARE EYEBALLED.

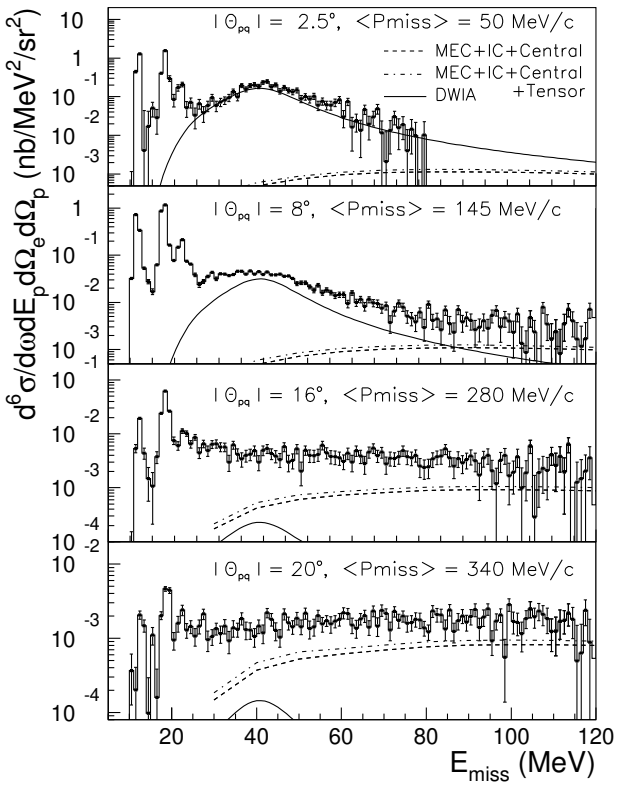

FIG. 13: $E_{\rm miss}$-dependence of the averaged measured cross sections as compared to DWIA calculations for $E_{\rm beam} = 2.442$ GeV. The cross sections shown are the average value of those measured on either side of $\vec{q}$ at each θ_{pq}. Error bars are statistical and on average, a 5.9% systematic uncertainty should be associated with the data points (see Tables XV through XIX). The solid lines in each panel show the $1s_{1/2}$-state single-particle strength calculated by Kelly [14] folded with the Lorentzian parametrization of Jeukenne and Mahaux [97]. The dashed line shows the calculations of Ryckebusch *et al.* [98] of the $(e,e'pn)$ and $(e,e'pp)$ contributions to the $(e,e'p)$ cross section including meson-exchange currents, intermediate $\Delta(1232)$ creation, and central correlations. The dot-dashed line also includes tensor correlations. WARNING: KELLY CALC IS OLD.

2. *Higher missing energy results*

Figure 13 presents averaged measured cross sections as a function of $E_{\rm miss}$ obtained at $E_{\rm beam} = 2.442$ GeV for four discrete HRS$_h$ angular settings from $2.5° < \theta_{pq} < 20°$, corresponding to average values of $P_{\rm miss}$ increasing from 50 MeV/c to 340 MeV/c. The cross section values shown are the averaged value of the cross sections measured on either side of $\vec{q}$. The strong peaks at $E_{\rm miss} =$ 12.1 and 18.3 MeV correspond to $1p$-shell proton removal, and have been discussed in detail in the previous section, as well as in [76]. For $E_{\rm miss} > 20$ MeV, the spectra behave in a completely different fashion. Qualitatively, in the top panel for $P_{\rm miss} \approx 50$ MeV/c, there is a broad and prominent peak centered at $E_{\rm miss} \approx 40$ MeV corresponding largely to the knockout of $1s_{1/2}$-state protons. As can be seen in the lower panels, the strength of this peak diminishes with increasing $P_{\rm miss}$, and has completely vanished beneath a flat background by $P_{\rm miss} \approx 280$ MeV/c. For $E_{\rm miss} > 60$ MeV and $P_{\rm miss} > 280$ MeV/c, the cross section decreases only very weakly as a function of $P_{\rm miss}$, and is completely independent of $E_{\rm miss}$.

In order to estimate how much of the cross section observed for $E_{\rm miss} > 25$ MeV can be explained by the single-particle knockout of protons from the $1s_{1/2}$-state, the data were compared to DWIA calculations by Kelly [14], identical to those previously discussed for the $1p$-shell data [WARNING OLD NONREL CALC IN THE FIGURES]. A spectroscopic factor of 0.73 with respect to the single-particle strength for the $1s_{1/2}$-state was chosen, and the cross sections (as well as the response functions) were spread over $E_{\rm miss}$ with the Lorentzian parametrization of Jeukenne and Mahaux [97]. This model describes both the cross section (see panels 1 and 2 of Figure 13) and the R_{L+TT} and R_T response functions (see Figures 14 and 15) rather well for $P_{\rm miss} < 145$ MeV/c, where there is clear $1s_{1/2}$-state peak at $E_{\rm miss} \approx 40$ MeV. At larger $P_{\rm miss}$, where there is no clear $1s_{1/2}$-state peak at $E_{\rm miss} \approx 40$ MeV, the data are much larger than the calculated cross section. The previously discussed relativistic single-particle calculations of Udías *et al.*, as well as

those of Pickelsimer *et al.* [7] demonstrate the same behavior. Thus, the larger $P_{\rm miss}$ data is not dominated by single-particle knockout.

The magnitude of $(S_T - S_L)$ [61] is consistent with that anticipated considering the measurements of Ulmer *et al.* [20] at $Q^2 = 0.14$ (GeV/c)^2 and Dutta *et al.* [27, 28] at $Q^2 = 0.6$ and 1.8 (GeV/c)^2. Together, these data suggest that transverse processes associated with the knockout of more than one nucleon decrease with increasing Q^2.

Also shown in Figure 13 are the calculations Ryckebusch *et al.* [98] for the $(e, e'pp)$ and $(e, e'pn)$ contributions to the $(e, e'p)$ cross section, performed within a Hartree-Fock framework. These two-particle knockout cross sections were calculated assuming the nucleons escaped the residual $A-2$ system without interacting inelastically with other nucleons - the spectator approximation. The calculation included pion-exchange currents, the creation of an intermediate $\Delta(1232)$, and both central and tensor short-range correlations. It predicts that, in these kinematics, the two-body pion-exchange and $\Delta(1232)$ currents account for roughly 85% of the calculated two-particle knockout strength, short-range tensor correlations account for about 13%, and short-range central correlations account for approximately 2%. The calculated two-particle knockout cross sections are essentially transverse in nature, since the two-body currents are predominantly transverse. The calculated strength underestimates the measured cross section by 50% but has the observed flat shape for $E_{\rm miss} > 50$ MeV. It is thus possible that heavier meson exchange and processes involving three (or more) nucleons need to be considered for a complete description of the data.

The separated continuum response functions for $P_{\rm miss}$ = 145 and 280 MeV/c are shown in Figures 14 and 15, respectively. Kinematic overlap enabled separations up to $E_{\rm miss} = 60$ MeV. It is generally accepted that excess strength at large $P_{\rm miss}$ should be transverse in nature if it is dominated by two-body currents rather than correlations [REF].

The separated response functions R_T, R_{L+TT}, and R_{LT} compared to DWIA calculations for $P_{\rm miss} = 145$ MeV/c are presented in Figure 14. The error bars are statistical and on average, an additional X.X% systematical uncertainty should be associated with the data points (see Tables XXIV and XXV). As previously mentioned, the Kelly [14] calculation was folded with the Lorentzian parametrization of Jeukenne and Mahaux [97] and binned in the same manner as the data. It does not reproduce the $E_{\rm miss}$-dependence of either R_T or R_L (not shown here). For $E_{\rm miss} > 50$ MeV, R_{L+TT} (which is essentially equal to R_L since $\frac{v_{TT}}{v_L} R_{TT}$ is roughly 7% of R_L in these kinematics [14]) is consistent with both the calculation and with zero, while R_T is significantly larger than both the calculation and zero out to $E_{\rm miss} =$ (at least) 60 MeV. R_{LT} is about twice the magnitude of the calculation over the entire $E_{\rm miss}$ range. Further, since R_{LT} is non-zero for $50 < E_{\rm miss} < 60$ MeV, R_L must also be non-zero over this range.

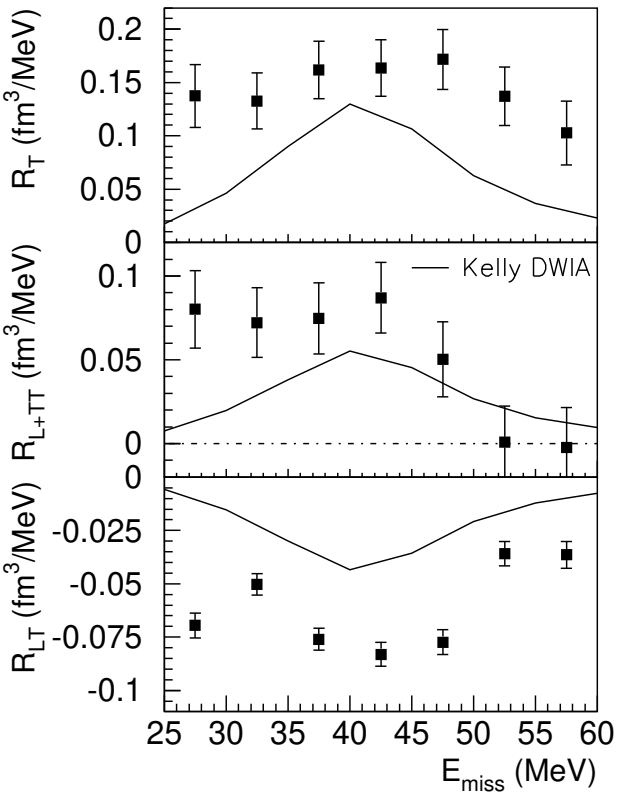

FIG. 14: $E_{\rm miss}$-dependence of the measured R_T, R_{L+TT}, and R_{LT} response functions compared to DWIA calculations for $< P_{\rm miss} > = 145$ MeV/c. Error bars are statistical only and on average, an additional X.X% systematic uncertainty should be associated with the data points (see Tables XXIV and XXV). The solid lines represent the calculations of Kelly [14] which have been folded with the Lorentzian parametrization of Jeukenne and Mahaux [97] and binned in the same manner as the data. WARNING: KELLY CALC IS OLD.

The separated response functions R_T, R_{L+TT}, and R_{LT} compared to DWIA calculations for $P_{\rm miss} = 280$ MeV/c are presented in Figure 14. The error bars are statistical and on average, an additional X.X% systematical uncertainty should be associated with the data points (see Tables XXIV and XXV). The Kelly calculation has again been folded with the Lorentzian parametrization of Jeukenne and Mahaux [97] and binned in the same manner as the data. None of the response functions show the broad peak centered at $E_{\rm miss} \approx 40$ MeV corresponding to the knockout of $1s_{1/2}$-state protons. While both R_T and R_{LT} are much larger than the calculation, R_{L+TT} is consistent with both the zero and the calculation over the entire $E_{\rm miss}$ range. The fact that R_T is much larger than R_{LT} indicates the cross section is largely due to transverse two-body currents. Finally, since R_{LT} is nonzero, R_L (which is again essentially equal to R_{L+TT}) must also be nonzero.

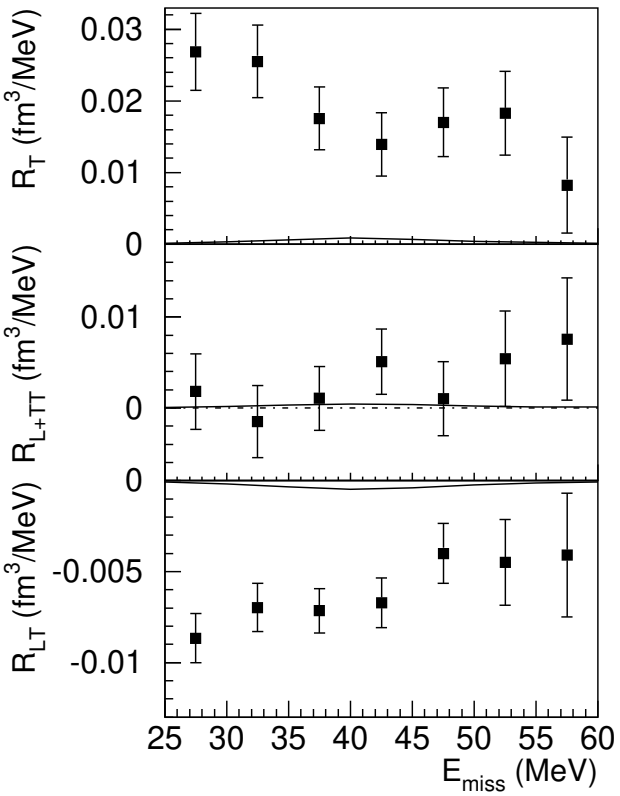

FIG. 15: $E_{\rm miss}$-dependence of the measured R_T, R_{L+TT}, and R_{LT} response functions compared to DWIA calculations for $< P_{\rm miss} > = 280$ MeV/c. Error bars are statistical only and on average, an additional X.X% systematic uncertainty should be associated with the data points (see Tables XXIV and XXV). The solid lines represent the calculations of Kelly [14] which have been folded with the Lorentzian parametrization of Jeukenne and Mahaux [97] and binned in the same manner as the data. WARNING: KELLY CALC IS OLD.

V. SUMMARY AND CONCLUSIONS

The ^{16}O$(e,e'p)$ reaction in quasielastic, constant (q,ω) kinematics at $Q^2 \approx 0.8$ (GeV/c)^2, $|\vec{q}| \approx 1$ GeV/c, and $\omega \approx 439$ MeV was measured for $0 < E_{\rm miss} < 120$ MeV and $0 < P_{\rm miss} < 350$ MeV/c. Five-fold differential cross sections for the removal of protons from the $1p$-shell have been obtained for $0 < P_{\rm miss} < 350$ MeV/c. Six-fold differential cross sections for $0 < E_{\rm miss} < 120$ MeV were obtained for $0 < P_{\rm miss} < 350$ MeV/c. These results were folded to extract the A_{LT} asymmetry and the R_L, R_T, R_{L+TT}, and R_{LT} response functions over a large range of $E_{\rm miss}$ and $P_{\rm miss}$.

Dynamic effects due to the inclusion of the lower components of the Dirac spinors in relativistic DWIA calculations are necessary to self-consistently reproduce the $1p$-shell A_{LT} and R_{LT} over the entire measured range of $P_{\rm miss}$. These calculations [17, 19, 94] do not include any two-body currents. The simultaneously strong agreement of the calculations with the cross section, A_{LT} asymmetry, and response function data, together with the calculations of Amaro *et al.* [95, 96], suggest such currents are already negligible at $Q^2 \approx 0.8$ (GeV/c)^2. Within the framework of the relativistic DWIA calculations, the three most important ingredients are the inclusion of both bound-nucleon and ejectile spinor distortion, the choice of bound-nucleon wave function, and the optical potential. Inclusion of the spinor distortion results in a diffractive wiggle in A_{LT} at $P_{\rm miss} = 325$ MeV/c which agrees nicely with the data. Varying the bound-nucleon wave function changes the $P_{\rm miss}$-location of this wiggle, but preserves the magnitude. Varying the optical potential changes the magnitude of the wiggle but preserves the $P_{\rm miss}$-location. Thus, mapping A_{LT} more precisely in the region $P_{\rm miss} > 200$ MeV/c shall create the opportunity to accurately determine the bound-state wave function, the optical potential, and the spectroscopic factors simultaneously. This experiment [99] has recently been performed in Hall A at Jefferson Lab, and the results are currently under analysis.

For $25 < E_{\rm miss} < 50$ MeV and $P_{\rm miss} < 145$ MeV/c, the reaction is dominated by the knockout of $1s_{1/2}$-state protons and is well-described by DWIA [14] calculations. As $P_{\rm miss}$ increases beyond 145 MeV/c, the single-particle aspect of the reaction diminishes. Cross sections and response functions are no longer peaked at $E_{\rm miss} = 40$ MeV, nor do they have the Lorenzian s-shell shape. Already at $P_{\rm miss} = 280$ MeV/c, the same DWIA calculations that did so well for $P_{\rm miss} < 145$ MeV/c underestimate the data by more than a decade. Thus, the single-particle aspect of the $1s_{1/2}$-state contributes $< 10\%$ to the cross section for $P_{\rm miss} > 280$ MeV/c. For the $1p$-shell, similar DWIA calculations described the data reasonably well up to $P_{\rm miss} = 340$ MeV/c.

For $25 < E_{\rm miss} < 120$ MeV and $P_{\rm miss} > 280$ MeV/c, the cross section is almost constant as a function of both $P_{\rm miss}$ and $E_{\rm miss}$. Two-nucleon calculations [98] account for only 50% of the magnitude of the data, but reproduce the shape well and account for the transverse nature for $E_{\rm miss} > 60$ MeV. This transverse nature suggests that two-body currents make a significant contribution to the excess strength observed in the continuum at higher $P_{\rm miss}$. The model, which accounts for the shape, transverse nature, and 50% of the measured cross section, predicts that the two-nucleon contributions are much larger than those of correlations. The 50% of the measured cross section that remains unaccounted for suggests additional currents and processes play an equally important role.

Acknowledgments

We acknowledge the outstanding support of the staff of the Accelerator and Physics Divisions at Jefferson Laboratory that made this experiment successful. We thank T. W. Donnelly, J. Ryckebusch, and J. W. Van Orden for providing theoretical calculations and for valuable discussions. This work was supported in part by the U. S. De-

partment of Energy contract DE-AC05-84ER40150 under which the Southeastern Universities Research Association (SURA) operates the Thomas Jefferson National Accelerator Facility, other Department of Energy contracts, the National Science Foundation, the Italian Istituto Nazionale di Fisica Nucleare (INFN), the French Atomic Energy Commission and National Center of Scientific Research, the Swedish Research Council, and the Natural Sciences and Engineering Research Council of Canada.

APPENDIX A: QUASIELASTIC RESULTS

1. Cross sections

a. 1p-*shell*

Five-fold differential cross sections for quasielastic proton knockout from the 1p-shell of ^{16}O are presented in Tables VIII and IX.

TABLE VIII: Measured cross sections for quasielastic proton knockout from the 1p-shell of ^{16}O for $< T_p > = 427$ MeV. Cuts were applied to remove the radiative tail from ^{1}H(e,ep) such that $< P_{\rm miss} > = 52.5$ MeV/c in each case. The $P_{\rm miss}$ bins were 20 MeV/c wide. While the HRS$_h$ was aligned along $\vec{q}$, this data set does not truly correspond to parallel kinematics because of these cuts. Since $\vec{p}_p$ and $\vec{q}$ had about the same magnitude, $\vec{P}_{\rm miss}$ arose from the slight angles between them, not from differences in their magnitudes. However, since the distribution of $\vec{P}_{\rm miss}$ was symmetrical about $\vec{q}$, the conditions of parallel kinematics are closely approximated.

		$1p_{1/2}$-state				$1p_{3/2}$-state			
$E_{\rm beam}$	θ_{pq}	$< Q^2 >$	$< \omega >$	$d^5\sigma/d\omega d\Omega_e d\Omega_p$	$\delta^{\rm sys}$	$< Q^2 >$	$< \omega >$	$d^5\sigma/d\omega d\Omega_e d\Omega_p$	$\delta^{\rm sys}$
(GeV)	(°)	(GeV/c)^2	(MeV)	(nb/MeV·sr^2)	(%)	(GeV/c)^2	(MeV)	(nb/MeV·sr^2)	(%)
0.843	0.0	0.810	436.0	0.0922 ± 0.0118	5.4	0.810	436.0	0.1143 ± 0.0115	5.4
1.643	0.0	0.820	421.5	0.5827 ± 0.0486	5.5	0.820	421.5	0.7418 ± 0.0514	5.4
2.442	0.0	0.815	423.0	1.5030 ± 0.1380	5.5	0.815	423.0	1.8540 ± 0.1500	5.5

TABLE IX: Measured cross sections for quasielastic proton knockout from the 1p-shell of ^{16}O for $< Q^2 > = 0.800$ (GeV/c)^2, $< \omega > = 436$ MeV, and $< T_p > = 427$ MeV. The $P_{\rm miss}$ bins were 20 MeV/c wide.

		$1p_{1/2}$-state			$1p_{3/2}$-state		
$E_{\rm beam}$	θ_{pq}	$< P_{\rm miss} >$	$d^5\sigma/d\omega d\Omega_e d\Omega_p$	$\delta^{\rm sys}$	$< P_{\rm miss} >$	$d^5\sigma/d\omega d\Omega_e d\Omega_p$	$\delta^{\rm sys}$
(GeV)	(°)	(MeV/c)	(nb/MeV·sr^2)	(%)	(MeV/c)	(nb/MeV·sr^2)	(%)
0.843	8.0	150.0	0.0789 ± 0.0057	5.6	150.0	0.1467 ± 0.0076	5.5
	16.0	275.0	0.0011 ± 0.0003	6.1	275.0	0.0058 ± 0.0006	7.2
1.643	-8.0	-148.0	0.2950 ± 0.0320	5.5	-146.0	0.5160 ± 0.0370	5.5
	8.0	148.0	0.5250 ± 0.0310	5.5	146.0	1.0390 ± 0.0360	5.4
2.442	-20.0	-355.0	0.0023 ± 0.0011	5.5	-355.0	0.0054 ± 0.0011	5.4
	-16.0	-279.0	0.0143 ± 0.0029	5.7	-275.0	0.0288 ± 0.0051	6.1
	-8.0	-149.0	0.9060 ± 0.0260	5.5	-149.0	1.5740 ± 0.0374	5.5
	-2.5	-60.0	1.5981 ± 0.0456	5.4	-60.0	2.2360 ± 0.0540	5.5
	2.5	60.0	1.5380 ± 0.0513	5.4	60.0	2.6210 ± 0.0650	5.5
	8.0	149.0	1.4605 ± 0.0261	5.5	149.0	2.9950 ± 0.0374	5.5
	16.0	279.0	0.0303 ± 0.0029	5.7	276.0	0.1672 ± 0.0051	6.2
	20.0	330.0	0.0057 ± 0.0005	5.6	330.0	0.0214 ± 0.0008	5.5

b. *Higher missing energies*

Six-fold differential cross sections for quasielastic proton knockout from ^{16}O for $E_{\rm miss} > 20$ MeV are presented in Tables X through XIX.

TABLE X: Measured cross sections for quasielastic proton knockout from ^{16}O for $E_{\rm beam} = 0.843$ GeV, $\theta_{pq} = 0.0°$, and $E_{\rm miss} > 20$ MeV. Cuts were applied to remove the radiative tail from ^{1}H(e,ep). The $P_{\rm miss}$ bins were 5 MeV/c wide. While the HRS$_h$ was aligned along $\vec{q}$, this data set does not truly correspond to parallel kinematics because of these cuts. Since $\vec{p}_p$ and $\vec{q}$ had about the same magnitude, $\vec{P}_{\rm miss}$ arose from the slight angles between them, not from differences in their magnitudes. However, since the distribution of $\vec{P}_{\rm miss}$ was symmetrical about $\vec{q}$, the conditions of parallel kinematics are closely approximated. A 5.8% systematic uncertainty is associated with these results.

$E_{\rm miss}$ (MeV)	$< \omega >$ (MeV)	$< Q^2 >$ $({\rm GeV}/c)^2$	$< P_{\rm miss} >$ (MeV/c)	$d^6\sigma/d\omega dE_p d\Omega_e d\Omega_p$ (nb/MeV^2/sr^2)
22.5	444.5	0.797	36.4	0.0082 ± 0.0007
27.5	445.2	0.796	38.7	0.0024 ± 0.0005
32.5	445.2	0.795	41.8	0.0085 ± 0.0008
37.5	445.8	0.794	45.0	0.0097 ± 0.0008
42.5	446.3	0.793	48.5	0.0113 ± 0.0009
47.5	447.7	0.790	51.3	0.0106 ± 0.0010
52.5	449.7	0.786	53.2	0.0065 ± 0.0010
57.5	451.7	0.782	55.5	0.0062 ± 0.0013

TABLE XI: Measured cross sections for quasielastic proton knockout from ^{16}O for $E_{\rm beam}$ = 0.843 GeV, θ_{pq} = 8.0°, and $E_{\rm miss}$ > 20 MeV. The $P_{\rm miss}$ bins were 5 MeV/c wide. A 6.0% systematic uncertainty is associated with these results.

$E_{\rm miss}$ (MeV)	$< \omega >$ (MeV)	$< Q^2 >$ $({\rm GeV}/c)^2$	$< P_{\rm miss} >$ (MeV/c)	$d^6\sigma/d\omega dE_p d\Omega_e d\Omega_p$ (nb/MeV^2/sr^2)
20.5	444.5	0.797	142.7	0.0019 ± 0.0017
21.5	444.9	0.796	143.5	0.0074 ± 0.0013
22.5	444.9	0.796	143.2	0.0104 ± 0.0018
23.5	445.0	0.795	143.2	0.0116 ± 0.0017
24.5	444.9	0.796	143.3	0.0021 ± 0.0012
25.5	444.9	0.796	143.3	0.0048 ± 0.0013
26.5	444.6	0.796	143.5	0.0019 ± 0.0010
27.5	445.2	0.795	143.8	0.0008 ± 0.0009
28.5	444.8	0.796	143.5	0.0041 ± 0.0011
29.5	444.6	0.796	143.9	0.0024 ± 0.0010
30.5	444.7	0.796	143.9	0.0022 ± 0.0009
31.5	444.9	0.796	144.2	0.0022 ± 0.0009
32.5	444.8	0.796	144.0	0.0041 ± 0.0010
33.5	445.0	0.795	144.6	0.0023 ± 0.0009
34.5	445.0	0.795	144.5	0.0013 ± 0.0008
35.5	444.9	0.796	144.7	0.0031 ± 0.0009
36.5	445.0	0.796	145.0	0.0018 ± 0.0008
37.5	445.1	0.796	145.1	0.0042 ± 0.0010
38.5	444.9	0.796	145.9	0.0013 ± 0.0008
39.5	444.9	0.796	145.6	0.0038 ± 0.0010
40.5	445.0	0.796	146.2	0.0027 ± 0.0009
41.5	444.9	0.796	146.2	0.0030 ± 0.0008
42.5	445.1	0.795	146.4	0.0029 ± 0.0009
43.5	445.1	0.795	147.3	0.0016 ± 0.0008
44.5	444.6	0.796	147.1	0.0020 ± 0.0008
45.5	445.4	0.795	147.6	0.0023 ± 0.0008
46.5	446.1	0.793	147.8	0.0028 ± 0.0009
47.5	446.5	0.793	148.0	0.0040 ± 0.0010
48.5	447.1	0.791	148.4	0.0016 ± 0.0009
49.5	447.5	0.790	148.5	0.0033 ± 0.0010
50.5	448.0	0.789	149.3	0.0029 ± 0.0010
51.5	448.5	0.789	149.5	0.0015 ± 0.0009
52.5	449.0	0.787	149.8	0.0013 ± 0.0007
53.5	449.4	0.786	150.0	0.0024 ± 0.0007
54.5	450.0	0.785	151.1	0.0022 ± 0.0009
55.5	450.5	0.784	151.2	0.0008 ± 0.0008
56.5	451.1	0.783	151.7	0.0019 ± 0.0010
57.5	451.6	0.782	151.7	0.0010 ± 0.0010
58.5	452.0	0.782	152.7	0.0007 ± 0.0009
59.5	452.5	0.781	152.6	0.0016 ± 0.0011

TABLE XII: Measured cross sections for quasielastic proton knockout from ^{16}O for $E_{\rm beam}$ = 0.843 GeV, θ_{pq} = 16.0°, and $E_{\rm miss}$ > 20 MeV. The $P_{\rm miss}$ bins were 5 MeV/c wide. A 5.9% systematic uncertainty is associated with these results.

$E_{\rm miss}$ (MeV)	$< \omega >$ (MeV)	$< Q^2 >$ $({\rm GeV}/c)^2$	$< P_{\rm miss} >$ (MeV/c)	$d^6\sigma/d\omega dE_p d\Omega_e d\Omega_p$ (nb/MeV^2/sr^2)
12.5	441.4	0.804	280.6	0.0004 ± 0.0001
17.5	444.0	0.799	281.7	0.0011 ± 0.0001
22.5	445.9	0.795	282.1	0.0005 ± 0.0001
27.5	446.0	0.795	281.6	0.0004 ± 0.0001
32.5	446.0	0.795	281.3	0.0003 ± 0.0001
37.5	445.9	0.795	281.2	0.0003 ± 0.0001
42.5	446.1	0.795	281.0	0.0002 ± 0.0001
47.5	448.1	0.790	281.8	0.0002 ± 0.0001
52.5	450.5	0.786	282.6	0.0003 ± 0.0001
57.5	452.8	0.781	283.6	0.0002 ± 0.0001

TABLE XIII: Measured cross sections for quasielastic proton knockout from ^{16}O for $E_{\rm beam}$ = 1.643 GeV, θ_{pq} = 0.0°, and $E_{\rm miss} > 20$ MeV. Cuts were applied to remove the radiative tail from ^{1}H(e,ep). The $P_{\rm miss}$ bins were 5 MeV/c wide. While the HRS$_h$ was aligned along $\vec{q}$, this data set does not truly correspond to parallel kinematics because of these cuts. Since $\vec{p}_p$ and $\vec{q}$ had about the same magnitude, $\vec{P}_{\rm miss}$ arose from the slight angles between them, not from differences in their magnitudes. However, since the distribution of $\vec{P}_{\rm miss}$ was symmetrical about $\vec{q}$, the conditions of parallel kinematics are closely approximated. A 5.8% systematic uncertainty is associated with these results.

$E_{\rm miss}$ (MeV)	$<\omega>$ (MeV)	$<Q^2>$ (GeV/c)^2	$<P_{\rm miss}>$ (MeV/c)	$d^6\sigma/d\omega dE_p d\Omega_e d\Omega_p$ (nb/MeV^2/sr^2)
27.5	450.0	0.795	62.5	0.0195 ± 0.0013
32.5	450.0	0.795	62.5	0.0293 ± 0.0012
37.5	450.0	0.795	62.5	0.0483 ± 0.0013
42.5	450.0	0.795	62.5	0.0534 ± 0.0014
47.5	450.0	0.795	62.5	0.0445 ± 0.0014
52.5	450.0	0.795	65.0	0.0263 ± 0.0015
57.5	450.0	0.795	67.5	0.0132 ± 0.0021

TABLE XIV: Measured cross sections for quasielastic proton knockout from ^{16}O for $E_{\rm beam}$ = 1.643 GeV, $|\theta_{pq}| = 8.0°$, and $E_{\rm miss} > 20$ MeV. The $P_{\rm miss}$ bins were 5 MeV/c wide. A 6.0% systematic uncertainty is associated with these results.

			$\theta_{pq} = +8.0°$		$\theta_{pq} = -8.0°$	
$E_{\rm miss}$ (MeV)	$<\omega>$ (MeV)	$<Q^2>$ (GeV/c)^2	$<P_{\rm miss}>$ (MeV/c)	$d^6\sigma/d\omega dE_p d\Omega_e d\Omega_p$ (nb/MeV^2/sr^2)	$<P_{\rm miss}>$ (MeV/c)	$d^6\sigma/d\omega dE_p d\Omega_e d\Omega_p$ (nb/MeV^2/sr^2)
20.5	431.5	0.807	137.6	0.1988 ± 0.0074	158.2	0.1163 ± 0.0041
21.5	432.7	0.807	138.4	0.0155 ± 0.0046	156.9	0.0240 ± 0.0027
22.5	433.7	0.805	139.1	0.0593 ± 0.0044	155.8	0.0160 ± 0.0021
23.5	434.4	0.806	140.6	0.0970 ± 0.0047	155.7	0.0507 ± 0.0026
24.5	436.1	0.804	141.6	0.0466 ± 0.0040	154.1	0.0294 ± 0.0023
25.5	436.2	0.804	141.8	0.0361 ± 0.0036	153.2	0.0163 ± 0.0020
26.5	438.0	0.802	142.7	0.0231 ± 0.0031	152.2	0.0130 ± 0.0018
27.5	439.0	0.802	144.1	0.0193 ± 0.0029	151.7	0.0079 ± 0.0016
28.5	439.5	0.802	144.9	0.0138 ± 0.0026	150.5	0.0060 ± 0.0015
29.5	441.2	0.800	146.6	0.0167 ± 0.0026	149.7	0.0117 ± 0.0016
30.5	441.7	0.800	146.8	0.0209 ± 0.0027	148.8	0.0132 ± 0.0016
31.5	442.4	0.801	147.5	0.0157 ± 0.0025	147.4	0.0101 ± 0.0015
32.5	443.6	0.799	148.8	0.0201 ± 0.0026	147.2	0.0075 ± 0.0014
33.5	445.1	0.798	149.9	0.0185 ± 0.0026	146.1	0.0098 ± 0.0014
34.5	445.8	0.796	151.3	0.0171 ± 0.0025	144.6	0.0138 ± 0.0015
35.5	446.9	0.796	151.1	0.0178 ± 0.0025	144.3	0.0109 ± 0.0015
36.5	447.5	0.796	151.9	0.0226 ± 0.0026	144.0	0.0135 ± 0.0015
37.5	448.9	0.795	153.8	0.0218 ± 0.0025	142.7	0.0128 ± 0.0015
38.5	450.0	0.796	154.5	0.0245 ± 0.0027	141.7	0.0139 ± 0.0016
39.5	450.6	0.795	155.1	0.0214 ± 0.0026	140.9	0.0151 ± 0.0016
40.5	451.5	0.795	156.0	0.0242 ± 0.0027	141.1	0.0128 ± 0.0015
41.5	452.0	0.793	156.6	0.0264 ± 0.0027	139.6	0.0144 ± 0.0016
42.5	453.7	0.792	158.1	0.0171 ± 0.0025	137.9	0.0173 ± 0.0017
43.5	454.9	0.791	159.3	0.0175 ± 0.0024	137.9	0.0144 ± 0.0016
44.5	456.3	0.791	160.9	0.0202 ± 0.0025	136.6	0.0142 ± 0.0016
45.5	456.6	0.791	160.4	0.0203 ± 0.0025	135.5	0.0166 ± 0.0016
46.5	457.4	0.789	161.3	0.0136 ± 0.0022	136.3	0.0149 ± 0.0016
47.5	459.0	0.788	162.5	0.0146 ± 0.0022	134.5	0.0162 ± 0.0016
48.5	459.9	0.788	163.7	0.0170 ± 0.0023	133.7	0.0127 ± 0.0015
49.5	461.1	0.787	164.6	0.0144 ± 0.0022	132.8	0.0125 ± 0.0015
50.5	462.3	0.787	165.6	0.0157 ± 0.0023	132.5	0.0138 ± 0.0016
51.5	462.8	0.786	166.4	0.0142 ± 0.0021	131.9	0.0110 ± 0.0015
52.5	464.5	0.785	168.0	0.0079 ± 0.0019	130.2	0.0130 ± 0.0015
53.5	464.6	0.785	168.4	0.0078 ± 0.0019	130.8	0.0093 ± 0.0014
54.5	465.5	0.784	169.3	0.0073 ± 0.0018	130.1	0.0112 ± 0.0014
55.5	466.4	0.785	170.1	0.0096 ± 0.0019	129.7	0.0109 ± 0.0015
56.5	467.0	0.784	170.5	0.0094 ± 0.0019	128.3	0.0069 ± 0.0013
57.5	467.3	0.783	171.1	0.0066 ± 0.0018	128.4	0.0078 ± 0.0013
58.5	468.2	0.783	171.0	0.0062 ± 0.0018	129.5	0.0070 ± 0.0013
59.5	468.3	0.782	171.8	0.0041 ± 0.0016	127.2	0.0097 ± 0.0014
60.5	469.2	0.782	173.1	0.0100 ± 0.0019	127.8	0.0070 ± 0.0013
61.5	469.3	0.782	172.9	0.0060 ± 0.0018	127.1	0.0036 ± 0.0012
62.5	470.6	0.782	173.9	0.0051 ± 0.0018	127.3	0.0085 ± 0.0014
63.5	469.9	0.782	173.6	0.0062 ± 0.0017	126.8	0.0040 ± 0.0012
64.5	471.0	0.781	174.7	0.0071 ± 0.0019	126.9	0.0065 ± 0.0013
65.5	471.2	0.780	174.5	0.0045 ± 0.0018	125.8	0.0043 ± 0.0013
66.5	472.1	0.779	175.5	0.0077 ± 0.0019	125.9	0.0056 ± 0.0013
67.5	472.6	0.780	175.9	0.0049 ± 0.0019	125.5	0.0019 ± 0.0012
68.5	473.4	0.779	177.2	0.0061 ± 0.0019	126.1	0.0049 ± 0.0013
69.5	473.3	0.779	177.0	0.0071 ± 0.0019	124.0	0.0022 ± 0.0012
70.5	474.4	0.778	177.9	0.0020 ± 0.0017	125.2	0.0056 ± 0.0013
71.5	474.5	0.779	178.7	0.0033 ± 0.0017	124.8	0.0034 ± 0.0013
72.5	474.9	0.778	178.4	0.0052 ± 0.0018	125.2	0.0066 ± 0.0015

73.5	475.1	0.778	179.0	0.0065 ± 0.0020	125.1	0.0046 ± 0.0014
74.5	476.3	0.777	179.6	0.0027 ± 0.0018	124.4	0.0032 ± 0.0013
75.5	476.2	0.776	180.3	0.0026 ± 0.0017	124.4	0.0046 ± 0.0014
76.5	477.1	0.776	181.4	0.0061 ± 0.0021	122.3	0.0005 ± 0.0012
77.5	477.6	0.776	181.7	0.0034 ± 0.0019	124.1	0.0016 ± 0.0013
78.5	478.2	0.777	182.7	0.0056 ± 0.0021	123.8	0.0013 ± 0.0014
79.5	478.9	0.775	183.1	0.0056 ± 0.0021	123.4	0.0054 ± 0.0016
80.5	479.1	0.774	183.3	0.0059 ± 0.0023	122.9	0.0040 ± 0.0016
81.5	479.6	0.776	184.1	0.0008 ± 0.0018	122.7	0.0039 ± 0.0017
82.5	480.1	0.775	185.1	0.0007 ± 0.0018	122.8	0.0029 ± 0.0016
83.5	480.6	0.776	185.2	0.0039 ± 0.0021	121.8	0.0022 ± 0.0016
84.5	481.1	0.773	185.8	0.0058 ± 0.0025	122.8	0.0018 ± 0.0016
85.5	481.6	0.775	186.3	0.0028 ± 0.0023	122.2	0.0039 ± 0.0019
86.5	482.1	0.775	187.1	0.0065 ± 0.0027	122.9	0.0003 ± 0.0018
87.5	482.8	0.772	187.6	0.0049 ± 0.0030	123.1	0.0029 ± 0.0021

TABLE XV: Measured cross sections for quasielastic proton knockout from ^{16}O for $E_{\rm beam}$ = 2.442 GeV, $\theta_{pq} = 0.0°$, and $E_{\rm miss} > 20$ MeV. Cuts were applied to remove the radiative tail from ^{1}H(e,ep). The $P_{\rm miss}$ bins were 5 MeV/c wide. While the HRS$_h$ was aligned along $\vec{q}$, this data set does not truly correspond to parallel kinematics because of these cuts. Since $\vec{p}_p$ and $\vec{q}$ had about the same magnitude, $\vec{P}_{\rm miss}$ arose from the slight angles between them, not from differences in their magnitudes. However, since the distribution of $\vec{P}_{\rm miss}$ was symmetrical about $\vec{q}$, the conditions of parallel kinematics are closely approximated. A 5.8% systematic uncertainty is associated with these results.

$E_{\rm miss}$ (MeV)	$<\omega>$ (MeV)	$<Q^2>$ (GeV/c)^2	$<P_{\rm miss}>$ (MeV/c)	$d^6\sigma/d\omega dE_p d\Omega_e d\Omega_p$ (nb/MeV^2/sr^2)
27.5	450.0	0.795	60.0	0.0552 ± 0.0042
32.5	450.0	0.795	60.0	0.0890 ± 0.0045
37.5	450.0	0.795	60.0	0.1387 ± 0.0050
42.5	450.0	0.795	60.0	0.1580 ± 0.0058
47.5	450.0	0.795	62.5	0.1348 ± 0.0062
52.5	450.0	0.795	65.0	0.0756 ± 0.0063
57.5	450.0	0.795	67.5	0.0402 ± 0.0084

TABLE XVI: Measured cross sections for quasielastic proton knockout from ^{16}O for $E_{\rm beam}$ = 2.442 GeV, $\theta_{pq} = -2.5°$, and $E_{\rm miss} > 20$ MeV. The $P_{\rm miss}$ bins were 5 MeV/c wide. A 5.9% systematic uncertainty is associated with these results.

$E_{\rm miss}$ (MeV)	$<\omega>$ (MeV)	$<Q^2>$ (GeV/c)^2	$<P_{\rm miss}>$ (MeV/c)	$d^6\sigma/d\omega dE_p d\Omega_e d\Omega_p$ (nb/MeV^2/sr^2)
10.5	435.0		37.5	0.0003 ± 0.0009
11.5	437.0		48.2	0.4537 ± 0.0440
12.5	436.9		47.8	1.2734 ± 0.0788
13.5	437.3		47.8	0.0041 ± 0.0396
14.5	438.2		47.7	0.0172 ± 0.0245
15.5	437.0		49.4	0.0511 ± 0.0210
16.5	437.0		49.6	0.0285 ± 0.0178
17.5	440.9		47.1	0.4077 ± 0.0360
18.5	443.0		46.6	1.5424 ± 0.0677
19.5	442.0		46.7	0.2966 ± 0.0500
20.5	443.5		47.1	0.0848 ± 0.0308
21.5	444.2		46.8	0.1721 ± 0.0319
22.5	445.3		46.7	0.2100 ± 0.0292
23.5	444.4		46.2	0.0520 ± 0.0229
24.5	445.7		46.9	0.0717 ± 0.0212
25.5	445.0		46.5	0.0330 ± 0.0182
26.5	446.5		46.8	0.0661 ± 0.0185
27.5	449.5		46.7	0.0388 ± 0.0173
28.5	449.3		45.3	0.0590 ± 0.0176
29.5	450.4		46.2	0.0955 ± 0.0192
30.5	450.8		45.1	0.0589 ± 0.0181
31.5	451.9		45.4	0.0733 ± 0.0180
32.5	452.1		45.0	0.0810 ± 0.0179
33.5	453.3		45.6	0.0944 ± 0.0192
34.5	454.5		45.2	0.1375 ± 0.0211
35.5	455.1		46.1	0.0984 ± 0.0209
36.5	454.9		46.1	0.1950 ± 0.0227
37.5	457.3		45.6	0.1566 ± 0.0232
38.5	458.4		45.8	0.1937 ± 0.0232
39.5	458.4		46.1	0.2052 ± 0.0251
40.5	459.3		46.5	0.1841 ± 0.0236
41.5	459.9		45.8	0.2354 ± 0.0252
42.5	461.3		45.9	0.2401 ± 0.0260
43.5	462.7		45.6	0.1791 ± 0.0247
44.5	462.6		46.6	0.2049 ± 0.0245
45.5	464.0		45.9	0.1401 ± 0.0223
46.5	464.7		46.9	0.1721 ± 0.0224

47.5	467.9	45.7	0.1457 ± 0.0217
48.5	467.7	45.9	0.1323 ± 0.0211
49.5	468.2	45.8	0.1469 ± 0.0211
50.5	471.1	45.3	0.0893 ± 0.0189
51.5	471.0	45.9	0.1008 ± 0.0185
52.5	473.1	46.3	0.0866 ± 0.0175
53.5	472.1	45.8	0.1037 ± 0.0183
54.5	474.6	45.7	0.0607 ± 0.0165
55.5	474.5	45.4	0.0766 ± 0.0163
56.5	473.8	46.8	0.0617 ± 0.0155
57.5	476.5	45.8	0.0606 ± 0.0155
58.5	477.4	46.6	0.0717 ± 0.0158
59.5	479.4	45.1	0.0837 ± 0.0168
60.5	481.5	45.5	0.0298 ± 0.0140
61.5	480.8	46.2	0.0748 ± 0.0156
62.5	480.6	47.7	0.0165 ± 0.0125
63.5	480.7	47.8	0.0240 ± 0.0118
64.5	481.1	47.6	0.0135 ± 0.0109
65.5	484.1	46.5	0.0471 ± 0.0127
66.5	482.4	46.6	0.0195 ± 0.0118
67.5	485.9	47.4	0.0297 ± 0.0121
68.5	484.4	48.7	0.0491 ± 0.0134
69.5	490.6	46.5	0.0118 ± 0.0116
70.5	489.5	47.6	0.0021 ± 0.0103
71.5	490.8	48.3	0.0136 ± 0.0103
72.5	491.7	47.9	0.0306 ± 0.0118
73.5	491.6	49.2	0.0156 ± 0.0113
74.5	493.1	49.6	0.0192 ± 0.0114
75.5	494.7	49.1	0.0040 ± 0.0101
76.5	493.8	49.2	0.0144 ± 0.0111
77.5	496.0	48.7	0.0098 ± 0.0118
78.5	497.1	48.8	0.0039 ± 0.0099
79.5	498.3	50.8	0.0103 ± 0.0124

TABLE XVII: Measured cross sections for quasielastic proton knockout from ^{16}O for $E_{\rm beam} = 2.442$ GeV, $|\theta_{pq}| = 8.0°$, and $E_{\rm miss} > 20$ MeV. The $P_{\rm miss}$ bins were 5 MeV/c wide. A 6.0% systematic uncertainty is associated with these results.

			$\theta_{pq} = +8.0°$		$\theta_{pq} = -8.0°$	
$E_{\rm miss}$ (MeV)	$<\omega>$ (MeV)	$<Q^2>$ (GeV/c)^2	$<P_{\rm miss}>$ (MeV/c)	$d^6\sigma/d\omega dE_p d\Omega_e d\Omega_p$ (nb/MeV^2/sr^2)	$<P_{\rm miss}>$ (MeV/c)	$d^6\sigma/d\omega dE_p d\Omega_e d\Omega_p$ (nb/MeV^2/sr^2)
10.5	419.2	0.794	130.0	0.0594 ± 0.0034	169.7	0.0050 ± 0.0010
11.5	424.3	0.806	140.0	1.1002 ± 0.0144	170.0	0.3694 ± 0.0064
12.5	426.8	0.804	142.5	0.4265 ± 0.0117	170.0	0.2541 ± 0.0063
13.5	428.7	0.797	142.5	0.0734 ± 0.0074	170.0	0.0348 ± 0.0041
14.5	430.1	0.790	140.0	0.0369 ± 0.0053	165.2	0.0183 ± 0.0029
15.5	428.5	0.794	140.0	0.0211 ± 0.0042	160.2	0.0128 ± 0.0023
16.5	429.6	0.802	140.5	0.0940 ± 0.0052	167.5	0.0314 ± 0.0025
17.5	430.2	0.804	147.5	1.3435 ± 0.0159	167.5	0.4072 ± 0.0068
18.5	430.5	0.803	147.5	1.5496 ± 0.0187	167.5	0.7864 ± 0.0099
19.5	431.7	0.801	147.5	0.2208 ± 0.0122	165.0	0.1070 ± 0.0065
20.5	433.2	0.796	147.5	0.0994 ± 0.0085	162.5	0.0568 ± 0.0046
21.5	433.2	0.797	147.5	0.2123 ± 0.0084	162.5	0.0845 ± 0.0043
22.5	434.6	0.800	150.0	0.2869 ± 0.0092	162.5	0.1402 ± 0.0049
23.5	435.7	0.797	152.5	0.0990 ± 0.0074	160.0	0.0512 ± 0.0040
24.5	436.5	0.796	152.5	0.0843 ± 0.0065	162.5	0.0461 ± 0.0035
25.5	438.1	0.793	150.0	0.0595 ± 0.0058	160.0	0.0174 ± 0.0030
26.5	439.6	0.791	152.5	0.0310 ± 0.0051	160.0	0.0165 ± 0.0027
27.5	440.5	0.791	155.0	0.0371 ± 0.0049	155.2	0.0190 ± 0.0026
28.5	441.7	0.789	155.0	0.0474 ± 0.0050	157.9	0.0249 ± 0.0027
29.5	442.3	0.789	152.8	0.0566 ± 0.0051	155.2	0.0306 ± 0.0028
30.5	443.4	0.788	155.0	0.0412 ± 0.0048	157.5	0.0221 ± 0.0027
31.5	444.4	0.792	157.5	0.0492 ± 0.0048	155.0	0.0318 ± 0.0028
32.5	446.6	0.788	160.0	0.0545 ± 0.0048	155.0	0.0247 ± 0.0027
33.5	447.8	0.789	160.0	0.0450 ± 0.0047	155.0	0.0289 ± 0.0027
34.5	448.0	0.788	160.0	0.0498 ± 0.0047	152.7	0.0291 ± 0.0027
35.5	449.5	0.784	160.0	0.0625 ± 0.0049	150.0	0.0294 ± 0.0027
36.5	449.1	0.784	160.0	0.0609 ± 0.0049	150.0	0.0309 ± 0.0027
37.5	452.1	0.786	162.5	0.0443 ± 0.0046	147.5	0.0357 ± 0.0028
38.5	452.7	0.788	162.5	0.0521 ± 0.0046	150.0	0.0413 ± 0.0029
39.5	453.7	0.785	165.0	0.0459 ± 0.0045	147.9	0.0336 ± 0.0028
40.5	454.1	0.783	165.0	0.0537 ± 0.0046	145.2	0.0359 ± 0.0028
41.5	454.6	0.784	165.0	0.0416 ± 0.0044	147.5	0.0368 ± 0.0028
42.5	456.7	0.783	165.0	0.0456 ± 0.0044	147.5	0.0431 ± 0.0030
43.5	456.9	0.782	167.8	0.0421 ± 0.0043	147.5	0.0350 ± 0.0028
44.5	457.3	0.780	170.0	0.0392 ± 0.0042	145.0	0.0382 ± 0.0028
45.5	457.8	0.784	167.5	0.0462 ± 0.0043	142.7	0.0335 ± 0.0028
46.5	458.3	0.781	170.0	0.0387 ± 0.0042	145.0	0.0330 ± 0.0028
47.5	459.8	0.779	172.5	0.0408 ± 0.0042	145.2	0.0326 ± 0.0027
48.5	460.4	0.782	170.0	0.0317 ± 0.0040	142.7	0.0331 ± 0.0027
49.5	461.6	0.783	175.0	0.0287 ± 0.0039	143.0	0.0217 ± 0.0025

50.5	463.6	0.779	172.8	0.0249 ± 0.0037	143.0	0.0274 ± 0.0026
51.5	463.5	0.780	175.0	0.0268 ± 0.0037	142.5	0.0257 ± 0.0025
52.5	463.1	0.784	172.8	0.0208 ± 0.0035	145.0	0.0222 ± 0.0025
53.5	465.2	0.778	172.5	0.0170 ± 0.0034	145.4	0.0191 ± 0.0024
54.5	466.2	0.779	175.0	0.0249 ± 0.0035	145.0	0.0214 ± 0.0024
55.5	468.5	0.782	180.0	0.0147 ± 0.0032	145.0	0.0175 ± 0.0023
56.5	468.6	0.778	180.0	0.0211 ± 0.0034	143.4	0.0160 ± 0.0022
57.5	469.3	0.779	177.5	0.0144 ± 0.0032	140.5	0.0181 ± 0.0022
58.5	471.3	0.774	182.5	0.0131 ± 0.0031	142.5	0.0149 ± 0.0022
59.5	472.3	0.778	180.0	0.0147 ± 0.0031	142.7	0.0145 ± 0.0022
60.5	472.3	0.778	177.5	0.0149 ± 0.0031	145.0	0.0143 ± 0.0021
61.5	474.9	0.780	185.0	0.0057 ± 0.0028	143.2	0.0131 ± 0.0021
62.5	473.8	0.781	185.0	0.0164 ± 0.0030	137.5	0.0156 ± 0.0021
63.5	475.9	0.784	187.5	0.0112 ± 0.0029	140.8	0.0087 ± 0.0020
64.5	477.0	0.783	185.0	0.0127 ± 0.0029	137.8	0.0105 ± 0.0020
65.5	477.6	0.784	185.0	0.0085 ± 0.0028	140.0	0.0081 ± 0.0019
66.5	477.2	0.777	187.5	0.0142 ± 0.0029	138.6	0.0089 ± 0.0019
67.5	477.0	0.781	190.0	0.0111 ± 0.0029	135.6	0.0086 ± 0.0019
68.5	480.2	0.780	187.5	0.0114 ± 0.0029	137.5	0.0077 ± 0.0018
69.5	480.0	0.782	187.5	0.0061 ± 0.0026	135.0	0.0089 ± 0.0019
70.5	481.1	0.778	190.0	0.0096 ± 0.0027	138.0	0.0074 ± 0.0018
71.5	481.7	0.778	192.5	0.0044 ± 0.0025	133.4	0.0030 ± 0.0016
72.5	481.7	0.781	192.5	0.0051 ± 0.0024	138.0	0.0080 ± 0.0018
73.5	482.8	0.782	192.5	0.0133 ± 0.0027	134.6	0.0058 ± 0.0018
74.5	484.8	0.781	192.8	0.0097 ± 0.0027	137.5	0.0063 ± 0.0018
75.5	485.0	0.779	197.2	0.0046 ± 0.0025	136.4	0.0057 ± 0.0017
76.5	484.6	0.773	195.0	0.0057 ± 0.0025	128.2	0.0036 ± 0.0016
77.5	485.5	0.781	192.5	0.0048 ± 0.0024	135.0	0.0030 ± 0.0016
78.5	488.2	0.781	195.3	0.0054 ± 0.0024	132.5	0.0070 ± 0.0017
79.5	488.6	0.782	197.5	0.0026 ± 0.0023	132.5	0.0033 ± 0.0016
80.5	490.3	0.785	195.3	0.0104 ± 0.0026	133.1	0.0077 ± 0.0017
81.5	489.1	0.785	197.5	0.0035 ± 0.0024	132.5	0.0048 ± 0.0017
82.5	492.5	0.782	197.8	0.0045 ± 0.0023	134.3	0.0043 ± 0.0017
83.5	492.3	0.782	197.5	0.0025 ± 0.0023	135.3	0.0027 ± 0.0016
84.5	492.6	0.778	200.0	0.0065 ± 0.0024	127.5	0.0072 ± 0.0017
85.5	495.2	0.787	200.0	0.0048 ± 0.0024	137.5	0.0024 ± 0.0016
86.5	495.6	0.790	202.5	0.0025 ± 0.0023	133.7	0.0021 ± 0.0016
87.5	498.7	0.787	200.0	0.0119 ± 0.0026	127.5	0.0021 ± 0.0016
88.5	499.6	0.785	200.0	0.0044 ± 0.0025	127.5	0.0033 ± 0.0016
89.5	497.7	0.784	202.5	0.0086 ± 0.0026	130.3	0.0008 ± 0.0016
90.5	497.8	0.781	202.5	0.0052 ± 0.0026	133.1	0.0031 ± 0.0017
91.5	499.1	0.782	202.5	0.0023 ± 0.0024	132.2	0.0029 ± 0.0018
92.5	500.8	0.789	202.5	0.0067 ± 0.0026	130.3	-0.0008 ± 0.0016
93.5	500.4	0.794	207.5	0.0060 ± 0.0026	132.8	0.0022 ± 0.0017
94.5	498.8	0.779	202.5	0.0059 ± 0.0026	128.8	-0.0003 ± 0.0017
95.5	498.8	0.775	202.5	0.0085 ± 0.0028	131.2	0.0021 ± 0.0017
96.5	499.6	0.782	205.0	0.0087 ± 0.0028	127.5	0.0049 ± 0.0019
97.5	499.2	0.790	210.0	0.0022 ± 0.0026	132.5	0.0038 ± 0.0019
98.5	501.6	0.782	205.0	0.0118 ± 0.0031	128.2	-0.0024 ± 0.0015
99.5	504.3	0.774	205.0	0.0080 ± 0.0029	125.7	0.0000 ± 0.0017
100.5	503.0	0.781	207.5	0.0031 ± 0.0027	127.5	0.0016 ± 0.0019
101.5	500.7	0.776	207.5	0.0105 ± 0.0031	126.7	0.0008 ± 0.0019
102.5	502.6	0.776	210.0	0.0021 ± 0.0028	125.4	0.0006 ± 0.0018
103.5	501.9	0.776	210.0	0.0030 ± 0.0028	130.0	-0.0013 ± 0.0017
104.5	504.8	0.780	207.5	0.0080 ± 0.0031	127.8	0.0016 ± 0.0019
105.5	503.6	0.774	210.0	0.0051 ± 0.0031	125.0	-0.0004 ± 0.0018
106.5	507.9	0.778	210.5	-0.0000 ± 0.0028	129.0	-0.0027 ± 0.0016
107.5	507.1	0.784	210.0	0.0112 ± 0.0034	127.5	0.0048 ± 0.0022
108.5	509.3	0.781	212.5	0.0036 ± 0.0032	125.0	0.0033 ± 0.0023
109.5	510.0	0.781	212.5	0.0047 ± 0.0032	124.0	-0.0014 ± 0.0019
110.5	510.0	0.779	212.5	0.0020 ± 0.0031	126.1	0.0028 ± 0.0022
111.5	510.0	0.782	212.5	0.0024 ± 0.0030	122.5	-0.0007 ± 0.0022
112.5	510.0	0.779	212.5	0.0046 ± 0.0033	122.5	0.0025 ± 0.0024
113.5	510.0	0.769	216.4	0.0114 ± 0.0038	117.5	0.0029 ± 0.0025
114.5	510.0	0.778	215.0	0.0095 ± 0.0040	120.2	-0.0013 ± 0.0021
115.5	510.0	0.777	215.0	0.0048 ± 0.0037	122.5	-0.0015 ± 0.0020
116.5	510.0	0.776	215.8	0.0018 ± 0.0034	121.0	0.0005 ± 0.0021
117.5	510.0	0.774	215.0	0.0017 ± 0.0033	121.4	0.0017 ± 0.0023
118.5	510.0	0.759	217.5	0.0127 ± 0.0045	113.6	0.0016 ± 0.0024
119.5	510.0	0.777	217.5	0.0078 ± 0.0046	122.5	0.0018 ± 0.0027

TABLE XVIII: Measured cross sections for quasielastic proton knockout from ^{16}O for $E_{\rm beam}$ = 2.442 GeV, $|\theta_{pq}| = 16.0°$, and $E_{\rm miss} > 20$ MeV. The $P_{\rm miss}$ bins were 5 MeV/c wide. A 5.8% systematic uncertainty is associated with these results.

			$\theta_{pq} = +16.0°$		$\theta_{pq} = -16.0°$	
$E_{\rm miss}$ (MeV)	$<\omega>$ (MeV)	$<Q^2>$ (GeV/c)^2	$<P_{\rm miss}>$ (MeV/c)	$d^6\sigma/d\omega dE_p d\Omega_e d\Omega_p$ (nb/MeV^2/sr^2)	$<P_{\rm miss}>$ (MeV/c)	$d^6\sigma/d\omega dE_p d\Omega_e d\Omega_p$ (nb/MeV^2/sr^2)
10.5	426.0	0.796	259.2	0.0002 ± 0.0002	296.9	0.0000 ± 0.0000
11.5	430.0	0.777	255.2	0.0050 ± 0.0005	286.6	0.0018 ± 0.0019
12.5	427.2	0.780	260.1	0.0312 ± 0.0012	290.0	0.0076 ± 0.0020

13.5	428.5	0.791	258.5	0.0069 ± 0.0008	290.2	0.0019 ± 0.0019
14.5	431.0	0.805	256.4	0.0023 ± 0.0006	290.8	0.0007 ± 0.0017
15.5	428.9	0.794	256.5	0.0019 ± 0.0005	290.1	0.0002 ± 0.0016
16.5	429.3	0.796	261.7	0.0037 ± 0.0005	290.0	0.0039 ± 0.0018
17.5	434.8	0.793	265.9	0.0376 ± 0.0012	281.8	0.0103 ± 0.0022
18.5	436.5	0.787	267.5	0.1008 ± 0.0021	281.2	0.0230 ± 0.0028
19.5	432.9	0.777	265.5	0.0432 ± 0.0017	281.8	0.0098 ± 0.0024
20.5	434.9	0.788	265.9	0.0118 ± 0.0012	284.1	0.0032 ± 0.0021
21.5	432.4	0.787	264.4	0.0096 ± 0.0010	281.7	0.0026 ± 0.0020
22.5	436.8	0.796	265.1	0.0152 ± 0.0010	282.9	0.0074 ± 0.0020
23.5	439.4	0.796	266.9	0.0143 ± 0.0010	280.3	0.0060 ± 0.0020
24.5	437.0	0.781	270.8	0.0100 ± 0.0009	281.4	0.0029 ± 0.0019
25.5	439.9	0.794	268.9	0.0078 ± 0.0008	282.1	0.0095 ± 0.0020
26.5	440.0	0.788	273.8	0.0076 ± 0.0008	278.1	0.0014 ± 0.0019
27.5	443.6	0.799	274.9	0.0053 ± 0.0007	280.4	0.0078 ± 0.0020
28.5	444.8	0.788	275.8	0.0054 ± 0.0007	276.0	0.0043 ± 0.0020
29.5	447.2	0.789	277.7	0.0075 ± 0.0007	278.0	0.0053 ± 0.0021
30.5	444.0	0.799	278.9	0.0054 ± 0.0007	279.0	0.0078 ± 0.0021
31.5	451.2	0.795	277.1	0.0047 ± 0.0006	273.6	0.0068 ± 0.0020
32.5	447.8	0.797	278.6	0.0036 ± 0.0006	277.3	0.0077 ± 0.0020
33.5	449.0	0.795	280.6	0.0045 ± 0.0006	273.8	0.0015 ± 0.0019
34.5	445.9	0.787	281.2	0.0059 ± 0.0007	277.1	0.0064 ± 0.0020
35.5	451.3	0.790	281.1	0.0036 ± 0.0006	275.1	0.0049 ± 0.0021
36.5	448.8	0.785	281.3	0.0044 ± 0.0006	272.1	0.0024 ± 0.0019
37.5	451.6	0.784	282.8	0.0039 ± 0.0006	271.3	0.0041 ± 0.0019
38.5	453.3	0.779	284.2	0.0046 ± 0.0006	268.3	0.0037 ± 0.0019
39.5	452.9	0.790	284.8	0.0039 ± 0.0006	270.9	0.0059 ± 0.0019
40.5	456.0	0.789	287.8	0.0033 ± 0.0006	268.4	0.0027 ± 0.0018
41.5	452.7	0.791	287.2	0.0041 ± 0.0006	270.6	0.0057 ± 0.0019
42.5	453.2	0.795	285.1	0.0039 ± 0.0006	270.3	0.0067 ± 0.0020
43.5	455.0	0.784	288.1	0.0028 ± 0.0005	268.5	0.0057 ± 0.0019
44.5	456.2	0.795	290.3	0.0033 ± 0.0005	267.3	0.0045 ± 0.0019
45.5	455.9	0.786	296.8	0.0025 ± 0.0005	267.7	0.0041 ± 0.0019
46.5	459.7	0.792	291.8	0.0039 ± 0.0005	266.6	0.0076 ± 0.0021
47.5	459.4	0.796	293.1	0.0038 ± 0.0006	266.1	0.0022 ± 0.0019
48.5	464.6	0.785	295.5	0.0024 ± 0.0005	262.6	0.0041 ± 0.0020
49.5	464.4	0.789	296.1	0.0037 ± 0.0005	261.9	0.0070 ± 0.0020
50.5	465.2	0.789	297.9	0.0025 ± 0.0005	261.3	0.0016 ± 0.0019
51.5	464.5	0.790	296.3	0.0028 ± 0.0005	262.8	0.0070 ± 0.0019
52.5	464.7	0.799	302.3	0.0026 ± 0.0005	266.3	0.0054 ± 0.0020
53.5	465.5	0.791	303.8	0.0029 ± 0.0005	260.3	0.0049 ± 0.0020
54.5	467.4	0.789	301.5	0.0030 ± 0.0005	262.0	0.0052 ± 0.0020
55.5	469.1	0.790	305.7	0.0021 ± 0.0005	261.5	0.0102 ± 0.0022
56.5	470.0	0.785	304.6	0.0030 ± 0.0005	257.8	0.0059 ± 0.0020
57.5	467.9	0.796	305.1	0.0027 ± 0.0005	261.5	0.0050 ± 0.0021
58.5	467.8	0.772	306.3	0.0018 ± 0.0005	255.0	0.0057 ± 0.0021
59.5	471.6	0.784	308.3	0.0025 ± 0.0005	256.8	0.0047 ± 0.0020
60.5	471.2	0.777	311.4	0.0024 ± 0.0005	255.8	0.0038 ± 0.0018
61.5	469.7	0.786	309.7	0.0034 ± 0.0005	258.0	0.0054 ± 0.0020
62.5	471.9	0.794	309.8	0.0021 ± 0.0005	261.4	0.0039 ± 0.0020
63.5	473.3	0.787	310.8	0.0025 ± 0.0005	254.8	0.0073 ± 0.0021
64.5	475.5	0.796	313.7	0.0025 ± 0.0005	256.4	0.0053 ± 0.0021
65.5	476.6	0.781	314.0	0.0025 ± 0.0005	254.4	0.0031 ± 0.0020
66.5	475.8	0.786	315.2	0.0024 ± 0.0005	253.3	0.0068 ± 0.0021
67.5	479.0	0.787	318.2	0.0023 ± 0.0005	252.4	0.0085 ± 0.0022
68.5	481.2	0.784	316.3	0.0029 ± 0.0005	252.3	0.0049 ± 0.0020
69.5	480.4	0.796	323.7	0.0023 ± 0.0005	252.6	0.0069 ± 0.0021
70.5	481.9	0.789	322.1	0.0024 ± 0.0005	251.0	0.0031 ± 0.0019
71.5	481.1	0.797	321.0	0.0025 ± 0.0005	254.5	0.0046 ± 0.0020
72.5	483.1	0.789	320.6	0.0023 ± 0.0005	249.5	0.0047 ± 0.0019
73.5	487.3	0.784	319.9	0.0023 ± 0.0005	249.1	0.0052 ± 0.0020
74.5	485.8	0.778	326.4	0.0028 ± 0.0005	249.1	0.0069 ± 0.0021
75.5	485.2	0.787	324.2	0.0024 ± 0.0005	252.5	0.0050 ± 0.0020
76.5	488.8	0.783	327.9	0.0020 ± 0.0004	246.8	0.0052 ± 0.0019
77.5	488.6	0.798	321.1	0.0017 ± 0.0004	251.0	0.0063 ± 0.0020
78.5	489.2	0.788	330.2	0.0030 ± 0.0005	245.7	0.0020 ± 0.0019
79.5	486.1	0.787	328.7	0.0019 ± 0.0005	245.9	0.0028 ± 0.0018
80.5	490.4	0.793	333.5	0.0023 ± 0.0005	247.2	0.0026 ± 0.0019
81.5	489.2	0.792	331.2	0.0018 ± 0.0004	247.6	0.0050 ± 0.0021
82.5	491.4	0.789	329.4	0.0017 ± 0.0004	247.6	0.0058 ± 0.0021
83.5	490.0	0.790	328.8	0.0021 ± 0.0005	248.7	0.0056 ± 0.0022
84.5	488.1	0.790	328.9	0.0024 ± 0.0005	249.8	0.0081 ± 0.0022
85.5	492.4	0.798	331.8	0.0016 ± 0.0005	247.5	0.0055 ± 0.0022
86.5	493.1	0.778	332.3	0.0025 ± 0.0005	243.7	0.0025 ± 0.0021
87.5	493.9	0.790	332.4	0.0024 ± 0.0005	245.7	0.0046 ± 0.0022
88.5	494.7	0.790	337.3	0.0023 ± 0.0005	246.7	0.0034 ± 0.0021
89.5	498.1	0.796	332.7	0.0024 ± 0.0005	246.7	0.0043 ± 0.0020
90.5	498.2	0.794	335.5	0.0026 ± 0.0005	242.4	0.0052 ± 0.0023
91.5	498.1	0.783	331.8	0.0015 ± 0.0005	242.0	0.0049 ± 0.0024
92.5	496.2	0.796	336.1	0.0027 ± 0.0005	250.8	0.0007 ± 0.0022
93.5	497.2	0.786	335.3	0.0018 ± 0.0005	244.6	0.0054 ± 0.0023
94.5	498.5	0.782	337.2	0.0010 ± 0.0005	244.4	0.0070 ± 0.0025
95.5	501.0	0.793	336.6	0.0032 ± 0.0006	239.6	0.0009 ± 0.0022

96.5	500.0	0.798	336.8	0.0012 ± 0.0005	244.8	0.0012 ± 0.0022
97.5	498.8	0.783	335.6	0.0021 ± 0.0006	241.8	0.0043 ± 0.0025
98.5	503.9	0.799	341.0	0.0016 ± 0.0006	247.4	0.0064 ± 0.0025
99.5	499.6	0.803	336.5	0.0014 ± 0.0005	243.3	0.0020 ± 0.0023
100.5	499.1	0.788	340.3	0.0027 ± 0.0006	243.4	0.0012 ± 0.0023
101.5	502.4	0.803	338.7	0.0015 ± 0.0006	244.4	0.0060 ± 0.0027
102.5	502.7	0.787	339.9	0.0022 ± 0.0006	238.9	-0.0002 ± 0.0026
103.5	506.8	0.803	339.6	0.0025 ± 0.0006	239.3	0.0012 ± 0.0025
104.5	500.3	0.799	342.0	0.0021 ± 0.0006	242.2	0.0099 ± 0.0033
105.5	507.9	0.795	344.3	0.0031 ± 0.0007	238.8	-0.0025 ± 0.0027
106.5	504.4	0.787	338.7	0.0017 ± 0.0006	239.4	0.0022 ± 0.0029
107.5	509.0	0.780	342.3	0.0020 ± 0.0007	239.8	0.0026 ± 0.0030
108.5	505.8	0.766	338.8	0.0017 ± 0.0007	235.7	0.0025 ± 0.0030
109.5	508.9	0.794	343.4	0.0026 ± 0.0007	244.6	0.0057 ± 0.0029
110.5	510.0	0.791	347.3	0.0018 ± 0.0007	245.4	0.0034 ± 0.0034
111.5	510.0	0.791	345.7	0.0019 ± 0.0007	242.8	0.0058 ± 0.0037
112.5	510.0	0.817	345.8	0.0033 ± 0.0009	244.8	0.0007 ± 0.0032
113.5	510.0	0.798	346.4	0.0020 ± 0.0009	241.7	0.0109 ± 0.0040
114.5	510.0	0.797	346.5	0.0027 ± 0.0009	243.6	-0.0036 ± 0.0032
115.5	510.0	0.792	346.5	0.0021 ± 0.0009	239.3	0.0004 ± 0.0033
116.5	510.0	0.802	350.2	0.0010 ± 0.0008	245.0	0.0019 ± 0.0036
117.5	510.0	0.797	350.6	0.0023 ± 0.0009	242.5	0.0018 ± 0.0040
118.5	510.0	0.794	346.9	0.0027 ± 0.0011	247.0	0.0046 ± 0.0043
119.5	510.0	0.804	350.4	0.0008 ± 0.0009	236.8	0.0002 ± 0.0036

TABLE XIX: Measured cross sections for quasielastic proton knockout from ^{16}O for $E_{\rm beam}$ = 2.442 GeV, $|\theta_{pq}| = 20.0°$, and $E_{\rm miss} > 20$ MeV. The $P_{\rm miss}$ bins were 5 MeV/c wide. A 5.9% systematic uncertainty is associated with these results.

			$\theta_{pq} = +20.0°$		$\theta_{pq} = -20.0°$	
$E_{\rm miss}$	$<\omega>$	$<Q^2>$	$<P_{\rm miss}>$	$d^6\sigma/d\omega dE_p d\Omega_e d\Omega_p$	$<P_{\rm miss}>$	$d^6\sigma/d\omega dE_p d\Omega_e d\Omega_p$
(MeV)	(MeV)	(GeV/c)^2	(MeV/c)	(nb/MeV^2/sr^2)	(MeV/c)	(nb/MeV^2/sr^2)
10.5	424.1	0.803	327.9	0.0001 ± 0.0001	364.0	0.0006 ± 0.0005
11.5	425.4	0.788	326.7	0.0003 ± 0.0001	358.4	0.0001 ± 0.0004
12.5	426.2	0.785	327.6	0.0036 ± 0.0003	357.1	0.0006 ± 0.0004
13.5	428.4	0.789	326.9	0.0025 ± 0.0003	354.4	0.0005 ± 0.0005
14.5	431.4	0.789	326.1	0.0002 ± 0.0002	356.9	0.0000 ± 0.0003
15.5	431.5	0.793	332.3	0.0002 ± 0.0001	355.3	0.0020 ± 0.0006
16.5	429.4	0.791	329.5	0.0001 ± 0.0001	355.0	0.0002 ± 0.0004
17.5	428.3	0.784	331.8	0.0037 ± 0.0003	353.7	0.0004 ± 0.0004
18.5	430.2	0.797	333.5	0.0091 ± 0.0005	356.0	0.0002 ± 0.0004
19.5	431.9	0.795	333.8	0.0074 ± 0.0005	355.3	0.0014 ± 0.0006
20.5	434.7	0.791	334.4	0.0021 ± 0.0004	351.9	-0.0002 ± 0.0003
21.5	437.6	0.778	336.8	0.0004 ± 0.0003	346.2	0.0028 ± 0.0007
22.5	438.0	0.785	334.3	0.0018 ± 0.0003	348.6	0.0030 ± 0.0007
23.5	436.8	0.787	336.7	0.0023 ± 0.0003	350.7	0.0003 ± 0.0005
24.5	435.3	0.790	337.4	0.0021 ± 0.0003	352.2	0.0008 ± 0.0005
25.5	440.2	0.787	339.4	0.0019 ± 0.0003	349.6	0.0002 ± 0.0005
26.5	439.3	0.790	340.7	0.0019 ± 0.0003	348.4	0.0011 ± 0.0006
27.5	441.4	0.796	346.8	0.0028 ± 0.0003	347.5	0.0015 ± 0.0006
28.5	441.7	0.792	345.5	0.0012 ± 0.0003	347.6	0.0007 ± 0.0005
29.5	440.0	0.791	345.6	0.0018 ± 0.0003	346.9	0.0003 ± 0.0004
30.5	445.7	0.793	346.7	0.0019 ± 0.0003	346.3	0.0009 ± 0.0004
31.5	446.0	0.808	346.5	0.0014 ± 0.0003	349.6	0.0009 ± 0.0005
32.5	447.7	0.792	349.3	0.0015 ± 0.0003	342.2	0.0014 ± 0.0006
33.5	447.8	0.804	346.5	0.0018 ± 0.0003	343.7	0.0001 ± 0.0005
34.5	447.3	0.798	347.1	0.0015 ± 0.0003	342.7	0.0013 ± 0.0006
35.5	449.6	0.789	353.8	0.0020 ± 0.0003	342.0	0.0006 ± 0.0005
36.5	451.2	0.785	351.4	0.0015 ± 0.0003	340.3	0.0022 ± 0.0006
37.5	450.7	0.793	352.2	0.0017 ± 0.0003	340.0	0.0009 ± 0.0006
38.5	451.7	0.794	356.7	0.0018 ± 0.0003	340.0	0.0008 ± 0.0006
39.5	454.1	0.781	356.9	0.0018 ± 0.0003	336.6	0.0003 ± 0.0005
40.5	454.0	0.786	357.4	0.0016 ± 0.0003	335.4	0.0013 ± 0.0005
41.5	455.0	0.783	358.1	0.0016 ± 0.0003	334.6	0.0008 ± 0.0006
42.5	455.8	0.784	357.6	0.0022 ± 0.0003	333.8	0.0022 ± 0.0006
43.5	457.4	0.797	359.5	0.0019 ± 0.0003	337.1	0.0017 ± 0.0006
44.5	459.5	0.787	363.2	0.0019 ± 0.0003	333.5	0.0006 ± 0.0006
45.5	459.2	0.802	363.4	0.0017 ± 0.0003	335.6	0.0003 ± 0.0005
46.5	459.1	0.791	366.9	0.0018 ± 0.0003	335.5	0.0024 ± 0.0007
47.5	459.8	0.783	364.0	0.0017 ± 0.0003	332.4	0.0015 ± 0.0006
48.5	459.9	0.792	366.4	0.0019 ± 0.0003	331.0	0.0009 ± 0.0005
49.5	461.8	0.784	366.1	0.0017 ± 0.0003	330.2	0.0020 ± 0.0007
50.5	465.7	0.788	369.0	0.0017 ± 0.0003	327.6	0.0012 ± 0.0006
51.5	463.5	0.789	365.5	0.0022 ± 0.0003	330.9	0.0021 ± 0.0007
52.5	464.9	0.793	367.3	0.0017 ± 0.0003	328.8	0.0010 ± 0.0007
53.5	465.3	0.789	374.3	0.0015 ± 0.0003	327.9	0.0014 ± 0.0007
54.5	467.2	0.789	371.9	0.0015 ± 0.0003	327.2	0.0026 ± 0.0006
55.5	467.0	0.785	374.0	0.0018 ± 0.0003	326.8	0.0013 ± 0.0006
56.5	468.8	0.785	376.0	0.0021 ± 0.0003	325.6	0.0014 ± 0.0005
57.5	472.0	0.788	374.1	0.0015 ± 0.0003	324.8	0.0016 ± 0.0007
58.5	471.2	0.779	375.0	0.0015 ± 0.0003	322.7	0.0018 ± 0.0006

59.5	471.4	0.779	376.5	0.0020 ± 0.0003	323.4	0.0016 ± 0.0006
60.5	472.9	0.784	377.0	0.0024 ± 0.0003	322.6	0.0020 ± 0.0007
61.5	472.3	0.792	378.6	0.0019 ± 0.0003	326.0	0.0024 ± 0.0007
62.5	473.6	0.789	377.8	0.0019 ± 0.0003	323.8	0.0011 ± 0.0007
63.5	475.0	0.791	380.8	0.0013 ± 0.0003	322.3	0.0015 ± 0.0007
64.5	476.0	0.785	381.2	0.0017 ± 0.0003	320.7	0.0019 ± 0.0006
65.5	478.8	0.789	385.5	0.0021 ± 0.0003	318.7	0.0020 ± 0.0007
66.5	478.8	0.790	382.1	0.0013 ± 0.0002	319.9	0.0015 ± 0.0006
67.5	481.5	0.786	384.7	0.0022 ± 0.0003	317.9	0.0025 ± 0.0007
68.5	480.0	0.791	387.0	0.0016 ± 0.0003	319.4	0.0014 ± 0.0008
69.5	480.3	0.788	387.5	0.0022 ± 0.0003	317.9	0.0026 ± 0.0008
70.5	480.9	0.782	383.3	0.0019 ± 0.0003	316.8	0.0024 ± 0.0006
71.5	481.3	0.786	387.5	0.0013 ± 0.0003	319.5	0.0012 ± 0.0007
72.5	482.5	0.792	394.3	0.0021 ± 0.0003	315.8	0.0025 ± 0.0007
73.5	486.6	0.791	393.4	0.0014 ± 0.0003	316.3	0.0021 ± 0.0007
74.5	486.2	0.781	395.4	0.0028 ± 0.0004	313.6	0.0012 ± 0.0006
75.5	485.3	0.792	393.4	0.0014 ± 0.0003	318.2	0.0018 ± 0.0007
76.5	485.0	0.787	393.7	0.0014 ± 0.0002	315.4	0.0019 ± 0.0007
77.5	487.0	0.798	396.2	0.0014 ± 0.0003	319.1	0.0022 ± 0.0008
78.5	486.4	0.798	396.0	0.0017 ± 0.0003	320.9	0.0018 ± 0.0008
79.5	488.3	0.785	398.3	0.0023 ± 0.0003	312.8	0.0005 ± 0.0005
80.5	488.4	0.801	396.4	0.0019 ± 0.0003	315.2	0.0006 ± 0.0005
81.5	489.0	0.790	398.5	0.0018 ± 0.0003	313.5	0.0028 ± 0.0008
82.5	494.0	0.801	399.2	0.0021 ± 0.0003	315.3	0.0020 ± 0.0008
83.5	492.1	0.786	398.9	0.0017 ± 0.0003	313.3	0.0024 ± 0.0008
84.5	493.7	0.791	400.6	0.0022 ± 0.0003	314.9	0.0004 ± 0.0007
85.5	495.2	0.798	400.1	0.0025 ± 0.0003	313.6	0.0023 ± 0.0008
86.5	496.6	0.798	401.9	0.0018 ± 0.0003	310.4	0.0007 ± 0.0006
87.5	501.1	0.805	402.1	0.0015 ± 0.0003	311.9	0.0019 ± 0.0008
88.5	499.0	0.790	401.4	0.0015 ± 0.0003	306.8	0.0025 ± 0.0008
89.5	500.1	0.789	402.5	0.0020 ± 0.0003	306.3	0.0013 ± 0.0007
90.5	496.2	0.796	402.3	0.0018 ± 0.0003	311.2	0.0021 ± 0.0009
91.5	497.4	0.789	404.9	0.0019 ± 0.0003	308.8	0.0030 ± 0.0009
92.5	497.1	0.799	402.5	0.0022 ± 0.0003	313.8	0.0006 ± 0.0009
93.5	499.7	0.780	404.7	0.0015 ± 0.0003	307.9	0.0023 ± 0.0009
94.5	500.9	0.789	409.6	0.0018 ± 0.0004	307.4	0.0032 ± 0.0008
95.5	503.8	0.797	407.5	0.0019 ± 0.0004	306.9	-0.0001 ± 0.0006
96.5	502.5	0.797	407.1	0.0021 ± 0.0004	309.5	0.0013 ± 0.0007
97.5	501.8	0.786	407.3	0.0015 ± 0.0004	306.1	0.0026 ± 0.0008
98.5	503.8	0.790	405.6	0.0018 ± 0.0004	311.0	-0.0007 ± 0.0007
99.5	504.3	0.794	407.4	0.0015 ± 0.0003	308.6	0.0042 ± 0.0011
100.5	501.5	0.797	406.2	0.0016 ± 0.0004	309.0	0.0018 ± 0.0010
101.5	505.3	0.790	409.4	0.0010 ± 0.0003	306.1	0.0023 ± 0.0010
102.5	503.3	0.801	408.5	0.0020 ± 0.0004	310.8	0.0003 ± 0.0009
103.5	506.0	0.796	407.7	0.0010 ± 0.0004	310.1	0.0027 ± 0.0009
104.5	507.6	0.795	413.0	0.0028 ± 0.0005	305.8	0.0022 ± 0.0011
105.5	506.7	0.788	411.3	0.0023 ± 0.0005	304.2	0.0016 ± 0.0011
106.5	508.3	0.802	414.0	0.0018 ± 0.0004	306.7	0.0029 ± 0.0011
107.5	511.2	0.807	411.2	0.0015 ± 0.0004	309.6	0.0027 ± 0.0012
108.5	510.2	0.815	413.3	0.0016 ± 0.0005	306.3	0.0021 ± 0.0013
109.5	508.6	0.786	412.4	0.0023 ± 0.0005	308.9	0.0002 ± 0.0010
110.5	508.1	0.782	414.1	0.0022 ± 0.0005	306.7	0.0003 ± 0.0012
111.5	512.0	0.794	411.7	0.0007 ± 0.0004	302.8	0.0027 ± 0.0014
112.5	509.1	0.801	411.4	0.0022 ± 0.0006	306.0	0.0013 ± 0.0011
113.5	512.4	0.803	419.0	0.0018 ± 0.0005	305.4	0.0025 ± 0.0013
114.5	510.3	0.790	419.1	0.0028 ± 0.0007	304.2	0.0008 ± 0.0015
115.5	512.7	0.804	416.9	0.0010 ± 0.0006	309.8	-0.0000 ± 0.0019
116.5	515.0	0.799	417.0	0.0008 ± 0.0005	304.5	0.0004 ± 0.0017
117.5	515.0	0.810	417.7	0.0021 ± 0.0007	310.4	0.0027 ± 0.0016
118.5	515.0	0.771	415.4	0.0004 ± 0.0006	300.5	0.0014 ± 0.0017
119.5	515.0	0.805	418.8	0.0012 ± 0.0008	311.8	-0.0001 ± 0.0027

2. Asymmetries and response functions

a. 1p-shell

Separated response functions (and asymmetries) for quasielastic proton knockout from ^{16}O are presented in Tables XX, XXI, and XXII.

TABLE XX: Separated response functions R_L and R_T for quasielastic proton knockout from the $1p$-shell of ^{16}O for $< T_p > = 427$ MeV. Cuts were applied to remove the radiative tail from ^{1}H(e, ep) such that $< P_{\rm miss} > = 52.5$ MeV/c in each case. The $P_{\rm miss}$ bins were 20 MeV/c wide. Note that the ω acceptance of the three measurements was shifted by about 3% in order to keep the phase space acceptance flat. The resulting change in the domain was taken as an additional 4% systematic uncertainty.

	$1p_{1/2}$-state					$1p_{3/2}$-state				
$< P_{\rm miss} >$	R_L	$\delta^{\rm sys}$	R_T	$\delta^{\rm sys}$	$< P_{\rm miss} >$	R_L	$\delta^{\rm sys}$	R_T	$\delta^{\rm sys}$
(MeV/c)	(fm^3)	(%)	(fm^3)	(%)	(MeV/c)	(fm^3)	(%)	(fm^3)	(%)
52.5	1.82 ± 1.17	999	7.58 ± 1.42	999	52.5	2.35 ± 1.18	999	9.40 ± 1.39	999

TABLE XXI: Separated response functions R_{L+TT} and R_T for quasielastic proton knockout from the $1p$-shell of ^{16}O for $< Q^2 > = 0.800$ (GeV/c)^2, $< \omega > = 436$ MeV, and $< T_p > = 427$ MeV. The $P_{\rm miss}$ bins were 20 MeV/c wide.

	$1p_{1/2}$-state					$1p_{3/2}$-state				
$< P_{\rm miss} >$	R_{L+TT}	$\delta^{\rm sys}$	R_T	$\delta^{\rm sys}$	$< P_{\rm miss} >$	R_{L+TT}	$\delta^{\rm sys}$	R_T	$\delta^{\rm sys}$
(MeV/c)	(fm^3)	(%)	(fm^3)	(%)	(MeV/c)	(fm^3)	(%)	(fm^3)	(%)
149.0	0.56 ± 0.49	999	6.08 ± 0.61	999	149.0	2.20 ± 0.75	999	10.35 ± 1.04	999
279.0	0.01 ± 0.03	999	0.12 ± 0.04	999	276.0	0.20 ± 0.06	999	0.29 ± 0.08	999

TABLE XXII: Separated asymmetries A_{LT} and response functions R_{LT} for quasielastic proton knockout from the $1p$-shell of ^{16}O for $< Q^2 > = 0.800$ (GeV/c)^2, $< \omega > = 436$ MeV, and $< T_p > = 427$ MeV. Save for the data labelled [*] which were obtained at $E_{\rm beam} = 1.643$ GeV, the beam energy was 2.442 GeV. The $P_{\rm miss}$ bins were 20 MeV/c wide. The agreement within statistical uncertainty of the bound-state A_{LT} asymmetry and R_{LT} response functions at the two beam energies reinforces our confidence in our evaluation of the systematic uncertainties in the cross section measurements.

	$1p_{1/2}$-state					$1p_{3/2}$-state				
$< P_{\rm miss} >$	A_{LT}	$\delta^{\rm sys}$	R_{LT}	$\delta^{\rm sys}$	$< P_{\rm miss} >$	A_{LT}	$\delta^{\rm sys}$	R_{LT}	$\delta^{\rm sys}$
(MeV/c)		(%)	(fm^3)	(%)	(MeV/c)		(%)	(fm^3)	(%)
60.0	0.02 ± 0.02	999	0.117 ± 0.134	999	60.0	-0.08 ± 0.02	999	-0.754 ± 0.165	999
148.0[*]	-0.25 ± 0.02	999	-1.198 ± 0.235	999	147.0[*]	-0.31 ± 0.04	999	-2.820 ± 0.292	999
149.0	-0.23 ± 0.02	999	-0.999 ± 0.066	999	148.0	-0.31 ± 0.01	999	-2.560 ± 0.096	999
279.0	-0.36 ± 0.08	999	-0.029 ± 0.007	999	276.0	-0.69 ± 0.04	999	-0.250 ± 0.013	999
345.0	-0.13 ± 0.22	999	-0.002 ± 0.003	999	345.0	-0.39 ± 0.08	999	-0.015 ± 0.003	999

b. Higher missing energies

Separated response functions (and asymmetries) for quasielastic proton knockout from ^{16}O for $E_{\rm miss} >$ XX MeV are presented in Tables XXIII through XXV.

TABLE XXIII: Separated response functions R_L and R_T for quasielastic proton knockout from ^{16}O at $\theta_{pq} = 0°$ for $E_{\rm miss} >$ XX MeV.

$< E_{\rm miss} >$	R_L	$\delta^{\rm sys}$	R_T	$\delta^{\rm sys}$	$S_T - S_L$	$\delta^{\rm sys}$
(MeV)	(fm^3/MeV)	(%)	(fm^3/MeV)	(%)	(10^{-10} MeV^{-4})	(%)
12.5	0.988 ± 0.068	999	0.827 ± 0.079	999	-105.56 ± 10.51	999
17.5	1.242 ± 0.152	999	1.095 ± 0.200	999	-131.41 ± 24.12	999
22.5	0.288 ± 0.098	999	0.442 ± 0.130	999	-21.93 ± 15.69	999
27.5	0.067 ± 0.050	999	0.203 ± 0.065	999	-0.47 ± 8.08	999
32.5	0.075 ± 0.044	999	0.346 ± 0.056	999	5.21 ± 7.13	999
37.5	0.141 ± 0.040	999	0.523 ± 0.049	999	3.66 ± 6.47	999
42.5	0.138 ± 0.037	999	0.600 ± 0.044	999	7.87 ± 6.03	999
47.5	0.100 ± 0.039	999	0.517 ± 0.047	999	9.77 ± 6.52	999
52.5	0.054 ± 0.044	999	0.304 ± 0.054	999	6.62 ± 7.38	999
57.5	-0.047 ± 0.111	999	0.253 ± 0.145	999	20.10 ± 19.06	999

TABLE XXIV: Separated response functions R_{L+TT} and R_T for quasielastic proton knockout from ^{16}O at $\theta_{pq} = 8°$ and $\theta_{pq} = 16°$ for $E_{\rm miss} >$ XX MeV.

	θ_{pq}=8°				θ_{pq}=16°			
$< E_{\rm miss} >$	R_{L+TT}	$\delta^{\rm sys}$	R_T	$\delta^{\rm sys}$	R_{L+TT}	$\delta^{\rm sys}$	R_T	$\delta^{\rm sys}$
(MeV/c)	(fm^3/MeV)	(%)	(fm^3/MeV)	(%)	(fm^3/MeV)	(%)	(fm^3/MeV)	(%)
12.5	0.259 ± 0.054	999	1.093 ± 0.069	999	-0.010 ± 0.005	999	0.035 ± 0.006	999
17.5	0.521 ± 0.067	999	1.709 ± 0.085	999	0.016 ± 0.007	999	0.066 ± 0.009	999
22.5	0.372 ± 0.037	999	0.550 ± 0.046	999	0.004 ± 0.005	999	0.034 ± 0.006	999
27.5	0.080 ± 0.023	999	0.137 ± 0.029	999	0.002 ± 0.004	999	0.027 ± 0.005	999
32.5	0.072 ± 0.021	999	0.133 ± 0.026	999	-0.001 ± 0.004	999	0.026 ± 0.005	999
37.5	0.075 ± 0.021	999	0.162 ± 0.027	999	0.001 ± 0.004	999	0.018 ± 0.004	999
42.5	0.087 ± 0.021	999	0.164 ± 0.026	999	0.005 ± 0.004	999	0.014 ± 0.004	999
47.5	0.050 ± 0.022	999	0.172 ± 0.028	999	0.001 ± 0.004	999	0.017 ± 0.005	999
52.5	0.001 ± 0.022	999	0.137 ± 0.027	999	0.005 ± 0.005	999	0.018 ± 0.006	999
57.5	-0.002 ± 0.024	999	0.010 ± 0.030	999	0.008 ± 0.007	999	0.008 ± 0.007	999

TABLE XXV: Separated asymmetries A_{LT} and response functions R_{LT} for quasielastic proton knockout from ^{16}O for at $\theta_{pq} = 8°$ and $\theta_{pq} = 16°$ for $E_{\rm miss} >$ XX MeV.

	θ_{pq}=8°				θ_{pq}=16°			
$< E_{\rm miss} >$	A_{LT}	$\delta^{\rm sys}$	R_{LT}	$\delta^{\rm sys}$	A_{LT}	$\delta^{\rm sys}$	R_{LT}	$\delta^{\rm sys}$
(MeV)		(%)	(fm^3/MeV)	(%)		(%)	(fm^3/MeV)	(%)
12.5		999	0.179 ± 0.013	999		999	0.005 ± 0.001	999
17.5		999	0.506 ± 0.014	999		999	0.038 ± 0.002	999
22.5		999	0.189 ± 0.010	999		999	0.015 ± 0.002	999
27.5		999	0.070 ± 0.006	999		999	0.009 ± 0.001	999
32.5		999	0.050 ± 0.005	999		999	0.007 ± 0.001	999
37.5		999	0.076 ± 0.005	999		999	0.007 ± 0.001	999
42.5		999	0.083 ± 0.006	999		999	0.007 ± 0.001	999
47.5		999	0.077 ± 0.006	999		999	0.004 ± 0.002	999
52.5		999	0.036 ± 0.006	999		999	0.004 ± 0.002	999
57.5		999	0.036 ± 0.006	999		999	0.004 ± 0.003	999

APPENDIX B: THE DIP-REGION INVESTIGATION

A small portion of the beam time allocated to the measurement discussed in the main text was used for an exploratory investigation of the "dip" region located in the energy transfer domain between the quasielastic peak and the Δ-resonance. For this investigation, $E_{\rm beam}$ = 1.643 GeV was employed, and the HRS$_e$ position and central momentum were fixed at $\theta_e = 37.17°$ and p_e = 1056 MeV/c, respectively. This resulted in $|\vec{q}| \approx 1.026$ GeV/c, $\omega \approx 589$ MeV, and $Q^2 = 0.706$ (GeV/c)^2 [113]. The HRS$_h$ was then positioned at $\theta_h = 38.45°$ (θ_{pq} = 0°) and its central momentum varied from 828 MeV/c to 1190 MeV/c in five steps of $\Delta p_p \approx 70$ MeV/c per step. These momentum settings were close enough to each other that there was adequate acceptance overlap between them to allow for radiative corrections to be performed.

The configuration of the experimental apparatus and data acquisition system was identical in all aspects to that used for the quasielastic measurement. The data analysis was also identical to that performed on the quasielastic data, save for an additional cut to remove contamination from H$(e,e'p)\pi^0$ events.

Figure 16 shows the measured cross sections for the dip region as a function of $E_{\rm miss}$ compared to calculations by Ryckebusch *et al.* [REF] for $E_{\rm beam}$ = 1.643 GeV (see Table XXVI). The error bars are statistical, and on average, an additional 5.8% systematic uncertainty should be associated with the data points. The dashed curve is a relativistic OMEA calculation (see the main text of this article for further details) for proton knockout from the $1s_{1/2}$-state in the IA and the solid curve is the same calculation plus the effects of MECs and ICs. The spectroscopic factor for these calculations was not fitted, but rather that which provided the best results for the quasielastic data was used (VALUE?). The dot-dashed curve illustrates the contributions of $(e,e'pn)$ and $(e,e'pp)$. The INVISIBLE CURVE shows the incoherent sum of the latter two curves. In general, the calculations underestimate the $1s_{1/2}$-state strength and overestimate the continuum strength. See the main text of this article for further details.

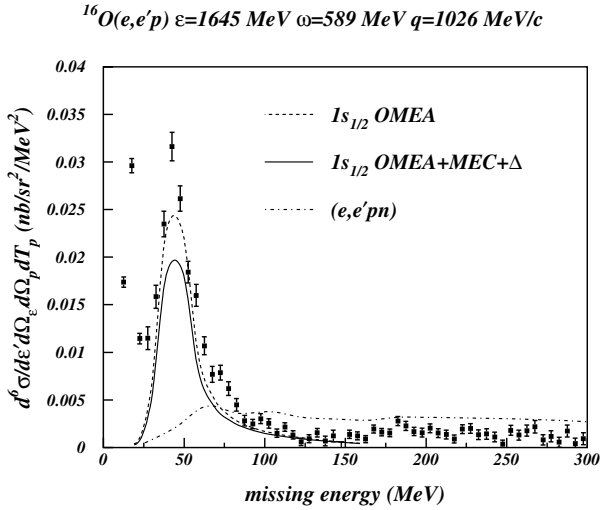

FIG. 16: What about adding a curve with the incoherent sum of the 1s1/2 and the two-nucleon knockout contribution ?

TABLE XXVI: Dip cross sections. Dip cross sections.

$E_{\rm miss}$	$< P_{\rm miss} >$	$d^6\sigma/d\omega dE_p d\Omega_e d\Omega_p$
(MeV)	(MeV)	(nb/MeV^2/sr^2)
12.5	175.0	0.0174 ± 0.0005
17.5	175.0	0.0296 ± 0.0007
22.5	170.0	0.0114 ± 0.0006
27.5	163.6	0.0115 ± 0.1191
32.5	152.1	0.0158 ± 0.1212
37.5	138.8	0.0235 ± 0.1343
42.5	132.8	0.0316 ± 0.1495
47.5	128.3	0.0262 ± 0.1328
52.5	119.4	0.0184 ± 0.1134
57.5	112.1	0.0160 ± 0.1149
62.5	107.5	0.0107 ± 0.0009
67.5	95.0	0.0078 ± 0.0009
72.5	95.0	0.0079 ± 0.0008
77.5	95.0	0.0062 ± 0.0007
82.5	90.0	0.0045 ± 0.0006

87.5	84.0	0.0028 ± 0.0005
92.5	76.0	0.0025 ± 0.0005
97.5	71.7	0.0030 ± 0.0005
102.5	68.0	0.0025 ± 0.0005
107.5	60.0	0.0015 ± 0.0004
112.5	61.4	0.0022 ± 0.0004
117.5	58.0	0.0013 ± 0.0004
122.5	51.0	0.0006 ± 0.0004
127.5	47.5	0.0010 ± 0.0004
132.5	50.0	0.0015 ± 0.0005
137.5	60.0	0.0007 ± 0.0005
142.5	45.0	0.0012 ± 0.0006
147.5	39.0	0.0002 ± 0.0004
152.5	39.3	0.0014 ± 0.0004
157.5	48.8	0.0012 ± 0.0004
162.5	51.7	0.0009 ± 0.0004
167.5	55.0	0.0019 ± 0.0004
172.5	62.0	0.0016 ± 0.0004
177.5	65.9	0.0015 ± 0.0004
182.5	69.0	0.0028 ± 0.0005
187.5	77.2	0.0023 ± 0.0005
192.5	94.0	0.0017 ± 0.0004
197.5	97.7	0.0016 ± 0.0005
202.5	97.7	0.0020 ± 0.0005
207.5	103.0	0.0015 ± 0.0005
212.5	114.1	0.0014 ± 0.0005
217.5	118.3	0.0009 ± 0.0004
222.5	122.3	0.0019 ± 0.0005
227.5	125.9	0.0020 ± 0.0005
232.5	135.0	0.0013 ± 0.0005
237.5	150.5	0.0014 ± 0.0006
242.5	157.7	0.0011 ± 0.0005
247.5	157.7	0.0004 ± 0.0004
252.5	167.0	0.0018 ± 0.0005
257.5	170.0	0.0013 ± 0.0005
262.5	173.2	0.0018 ± 0.0006
267.5	179.5	0.0022 ± 0.0006
272.5	185.9	0.0008 ± 0.0005
277.5	188.0	0.0012 ± 0.0006
282.5	210.0	0.0006 ± 0.0005
287.5	200.0	0.0017 ± 0.0006
292.5	200.0	0.0004 ± 0.0006
297.5	205.0	0.0009 ± 0.0006

[1] J. J. Kelly, Adv. Nucl. Phys. **23**, 75 (1996), and references therein.

[2] J. J. Kelly, Phys. Rev. C. **56**, 2672 (1997).

[3] S. Frullani and J. Mougey, Adv. Nucl. Phys. **14**, 1 (1984), and references therein.

[4] U. Amaldi et al., Phys. Lett. **25B**, 24 (1967).

[5] J. Mougey et al., Nucl. Phys. **A262**, 461 (1976).

[6] A. Picklesimer and J. W. Van Orden, Phys. Rev. C. **40**, 290 (1989).

[7] A. Picklesimer, J. W. Van Orden, and S. J. Wallace, Phys. Rev. C. **32**, 1312 (1985).

[8] H. Müther et al., Phys. Rev. C. **49**, R17 (1994).

[9] M. Bernheim et al., Nucl. Phys. **A375**, 381 (1982).

[10] L. Chinitz et al., Phys. Rev. Lett. **67**, 568 (1991).

[11] C. M. Spaltro et al., Phys. Rev. C. **48**, 2385 (1993).

[12] M. Leuschner et al., Phys. Rev. C. **49**, 955 (1994).

[13] K. I. Blomqvist et al., Phys. Lett. B. **344**, 85 (1995).

[14] J. J. Kelly, Phys. Rev. C. **60**, 044609 (1999), the calculations were revised using the NLSH wavefunctions.

[15] J. M. Udías et al., Phys. Rev. C. **48**, 2731 (1993).

[16] J. M. Udías et al., Phys. Rev. C. **51**, 3246 (1995).

[17] J. M. Udías et al., Phys. Rev. Lett. **83**, 5451 (1999).

[18] J. M. Udías and J. R. Vignote, Phys. Rev. C. **62**, 034302 (2000).

[19] J. M. Udías et al., private communication.

[20] P. E. Ulmer et al., Phys. Rev. Lett. **59**, 2259 (1987).

[21] R. Lourie et al., Phys. Rev. Lett. **56**, 2364 (1986).

[22] L. Weinstein et al., Phys. Rev. Lett. **64**, 1646 (1990).

[23] M. Holtrop et al., Phys. Rev. C. **58**, 3205 (1998).

[24] J. H. Morrison et al., Phys. Rev. C. **59**, 221 (1999).

[25] J. B. J. M. Lanen et al., Phys. Rev. Lett. **64**, 2250 (1990).

[26] G. van der Steenhoven et al., Nucl. Phys. **A480**, 547 (1988).

[27] D. Dutta et al., Phys. Rev. C. **61**, 061602(R) (2000).

[28] D. Dutta, Ph.D. thesis, Northwestern University (1999).

[29] T. Takaki et al., Phys. Rev. C. **39**, 359 (1989).

[30] J. Ryckebusch et al., Nucl. Phys. **A624**, 581 (1997).

[31] A. Gil et al., Nucl. Phys. **A627**, 599 (1997).

[32] A. Saha, W. Bertozzi, R. W. Lourie, and L. B. Weinstein, Experiment Proposal E89-003, Jefferson Laboratory (1989), see also `http://www.jlab.org/exp_prog/experiments/summaries/`.

[33] K. G. Fissum et al., MIT-LNS Internal Report 2/97, Massachusetts Institute of Technology (1997), see also `http://www.jlab.org/~fissum/e89003.html`.

[34] `http://hallaweb.jlab.org/`.

[35] `http://www.jlab.org/`.

[36] B. D. Anderson et al., to be submitted to Nucl. Instrum. Methods Phys. Res. Sect. A.

[37] *Hall A Operations Manual* (1991), see also `http://hallaweb.jlab.org/document/OPMAN/index.html`.

[38] W. Barry et al., Technical Memorandum JLAB-TN-90-246, Jefferson Laboratory (1990).

[39] W. Barry et al., Technical Memorandum JLAB-TN-91-087, Jefferson Laboratory (1991).

[40] F. Garibaldi et al., Nucl. Instrum. Methods Phys. Res. Sect. A **314**, 1 (1992).

[41] J. Gao et al., MIT-LNS Internal Report 4/98, Massachusetts Institute of Technology (1998), see also `http://www.jlab.org/~fissum/e89003/learned/e89003-beamdel.ps.gz`.

[42] K. B. Unser, IEEE Trans. Nuc. Sci. **16**, 934 (1969).

[43] K. B. Unser, IEEE Trans. Nuc. Sci. **28**, 2344 (1981).

[44] *Proceedings of the IEEE Particle Accelerator Conference in Chicago, Illinois* (1989).

[45] P. E. Ulmer, Internal Report to the E89-003 Collaboration (1998), see also `http://www.jlab.org/~fissum/e89003/learned/e89003-charge.ps.gz`.

[46] `http://www.aps.anl.gov/epics`.

[47] C. K. Sinclair, Technical Memorandum JLAB-TN-92-064, Jefferson Laboratory (1992).

[48] `http://hallaweb.jlab.org/equipment/high_resol.html`.

[49] N. Liyanage et al., MIT-LNS Internal Report 5/98, Massachusetts Institute of Technology (1998), see also `http://www.jlab.org/~fissum/e89003/learned/e89003-optics.ps.gz`.

[50] M. Liang, Technical Memorandum JLAB-TN-99-029, Jefferson Laboratory (1998), see also `http://www.jlab.org/~fissum/e89003/learned/survey_summary.ps.gz`.

[51] http://hallaweb.jlab.org/equipment/detectors/detectors.html; http://hallaweb.jlab.org/equipment/detectors/trig.html.

[52] K. G. Fissum et al., Nucl. Instrum. Methods Phys. Res. Sect. A **474**, 108 (2001).

[53] K. G. Fissum et al., Technical Memorandum JLAB-TN-00-016, Jefferson Laboratory (2000), see also http://www.jlab.org/~fissum/vdcs.html.

[54] M. Iodice et al., Nucl. Instrum. Methods Phys. Res. Sect. A **411**, 223 (1998), see also http://hallaweb.jlab.org/equipment/detectors/gas.html.

[55] http://hallaweb.jlab.org/equipment/acquisition.html.

[56] http://coda.jlab.org/.

[57] http://hallaweb.jlab.org/equipment/daq/dplot.html.

[58] http://wizard.mit.edu/~wwc/abacus.html.

[59] http://hallaweb.jlab.org/espace/index.html.

[60] J. Gao, Ph.D. thesis, Massachusetts Institute of Technology (1999).

[61] N. Liyanage, Ph.D. thesis, Massachusetts Institute of Technology (1999).

[62] R. Owens, Nucl. Instrum. Methods Phys. Res. Sect. A **288**, 574 (1990).

[63] L. B. Weinstein, Ph.D. thesis, Massachusetts Institute of Technology (1988).

[64] G. G. Simon et al., Nucl. Phys. **A333**, 381 (1980).

[65] L. E. Price et al., Phys. Rev. D. **4**, 45 (1971).

[66] http://www.jlab.org/~mliang/deadtime_cor/.

[67] E. Quint, Ph.D. thesis, University of Amsterdam (1998).

[68] R. Florizone, Ph.D. thesis, Massachusetts Institute of Technology (1999).

[69] E. Borie and D. Drechsel, Nucl. Phys. **A167**, 369 (1971).

[70] J. Templon et al., Phys. Rev. C. **61**, 014607 (2000).

[71] http://www.physics.odu.edu/~ulmer/mceep/mceep.html.

[72] A. S. Raskin and T. W. Donnelly, Ann. Phys. **191**, 78 (1989).

[73] J. J. Kelly, Adv. Nucl. Phys. **23**, 75 (1996).

[74] M. N. Rosenbluth, Phys. Rev. **79**, 615 (1950).

[75] K. G. Fissum and P. E. Ulmer, Technical Memorandum JLAB-TN-02-015, Jefferson Laboratory (2002), see also http://www.jlab.org/~fissum/e89003/learned/e89003_sysun_us.ps.gz.

[76] J. Gao et al., Phys. Rev. Lett. **84**, 3265 (2000).

[77] N. Liyanage et al., Phys. Rev. Lett. **86**, 5670 (2001).

[78] J. J. Kelly, Internal Report to the E89-003 Collaboration (1999), see also http://www.jlab.org/~fissum/e89003/publications/nfalt.ps.gz.

[79] J. J. Kelly, Phys. Rev. C. **59**, 3256 (1999).

[80] M. Hedayati-Poor, J. I. Johansson, and H. S. Sherif, Phys. Rev. C. **51**, 2044 (1995).

[81] T. de Forest Jr., Nucl. Phys. **A392**, 232 (1983).

[82] P. Mergell, U. G. Meiβner, and D. Dreschsel, Nucl. Phys. **A596**, 367 (1996).

[83] M. M. Sharma, M. A. Nagarajan, and P. Ring, Phys. Lett. B. **312**, 377 (1993).

[84] B. D. Serot and J. D. Walecka, Adv. Nucl. Phys. **16**, 1 (1986).

[85] E. D. Cooper, S. Hama, B. C. Clark, and R. L. Mercer, Phys. Rev. C. **47**, 297 (1993).

[86] J. M. Udías and J. R. Vignote, Internal Report to the E89-003 Collaboration (2001), see also http://www.jlab.org/~fissum/e89003/publications/udvig89003f.ps.gz.

[87] J. M. Udías et al., Phys. Rev. C. **64**, 024614 (2001), nucl-th/0101038.

[88] J. A. McNeil et al., Phys. Rev. C. **27**, 2123 (1983).

[89] C. J. Horowitz, Phys. Rev. C. **31**, 1340 (1985).

[90] D. P. Murdock, Phys. Rev. C. **35**, 1442 (1987).

[91] M. Gari and W. Krümplemann, Z. Phys. A. **322**, 689 (1985).

[92] D. H. Lu et al., Phys. Lett. B. **417**, 217 (1998).

[93] D. H. Lu et al., Phys. Rev. C. **60**, 068201 (1999).

[94] J. J. Kelly, private communication.

[95] J. E. Amaro et al., Phys. Rev. C. **60**, 014603 (1999).

[96] J. E. Amaro et al., private communication.

[97] J. P. Jeukenne and C. Mahaux, Nucl. Phys. **A394**, 445 (1983).

[98] S. Janssen et al., Nucl. Phys. **A672**, 285 (2000).

[99] A. Saha, W. Bertozzi, L. B. Weinstein, and K. G. Fissum, Experiment Proposal E00-102, Jefferson Laboratory (2000), see also http://www.jlab.org/exp_prog/experiments/summaries/ and http://www.jlab.org/~fissum/e00102/e00102.html.

[100] T. de Forest Jr., Ann. Phys. **45**, 365 (1967).

[101] Kinematically, an electron scattered through angle θ_e transfers momentum $\vec{q}$ and energy ω with $Q^2 = \vec{q}^2 - \omega^2$. The ejected proton has mass m_p, momentum $\vec{p}_p$, energy E_p, and kinetic energy T_p. In quasielastic kinematics, $\omega \approx Q^2/2m_p$. The cross section is typically measured as a function of missing energy $E_{\rm miss} = \omega - T_p - T_{\rm recoil}$ and missing momentum $P_{\rm miss} = |\vec{q} - \vec{p}_p|$. $T_{\rm recoil}$ is the kinetic energy of the residual nucleus. The lab polar angle between the ejected proton and virtual photon is θ_{pq} and the azimuthal angle is ϕ. $\theta_{pq} > 0^\circ$ corresponds to $\phi = 180^\circ$ and $\theta_p > \theta_q$. $\theta_{pq} < 0^\circ$ corresponds to $\phi = 0^\circ$.

[102] In the first Born approximation, the unpolarized $(e, e'p)$ cross section can be expressed as the sum of four independent response functions: R_L (longitudinal), R_T (transverse), R_{LT} (longitudinal-transverse interference, and R_{TT} (transverse-transverse interference).

[103] $A_{LT} \equiv \frac{\sigma(\phi=0^\circ)-\sigma(\phi=180^\circ)}{\sigma(\phi=0^\circ)+\sigma(\phi=180^\circ)}$. A_{LT} is a particularly useful quantity for experimentalists because it is systematically much less challenging to extract than either an absolute cross section or a structure function.

[104] The transverse-longitudinal difference is given by $S_T - S_L$, where $S_X = \sigma_{\rm Mott} V_X R_X / \sigma_X^{ep}$, and $X \epsilon \{T, L\}$. σ_X^{ep} represents components of the off-shell ep cross section and may be calculated using the CC1 or CC2 prescriptions of deForest [81, 100].

[105] When necessary, the differential dependencies of the measured cross sections were changed to match those employed in the theoretical calculations. The pristine detection volume $\Delta V_b(E_{\rm miss}, P_{\rm miss}, \omega, Q^2)$ was changed to a weighted detection volume by weighting each of the trials with the appropriate Jacobian(s).

[106] The difference between cross sections averaged over the spectrometer acceptances and calculated for a small region of the central kinematics was no more than 1%. Thus, the finite acceptance of the spectrometers was not an issue.

[107] This Jacobian is given by $\frac{\partial E_{\rm miss}}{\partial p_p} = \frac{p_p}{E_p} + \frac{\vec{p}_p \cdot \vec{p}_{\rm recoil}}{p_p E_{\rm recoil}}$, where $E_{\rm recoil} = \sqrt{p_{\rm recoil}^2 + m_{\rm recoil}^2}$.

[108] The kinematic factor $K = \frac{p_p E_p}{8\pi^3}$, while $\sigma_{\rm Mott} =$

$\frac{\alpha^2\cos^2(\theta_e/2)}{4E_0^2\sin^4(\theta_e/2)}$. The dimensionless kinematic factors are as follows: $v_L = \frac{Q^4}{\vec{q}^{\,4}}$, $v_T = \frac{Q^2}{2\vec{q}^{\,2}} + \tan^2(\theta_e/2)$, $v_{LT} = \frac{Q^2}{\vec{q}^{\,2}}\sqrt{\frac{Q^2}{\vec{q}^{\,2}} + \tan^2(\theta_e/2)}$, and $v_{TT} = \frac{Q^2}{2\vec{q}^{\,2}}$. The five-fold differential cross sections $\frac{d^5\sigma}{d\omega\ d\Omega_e\ d\Omega_p}$ for proton removal from the $1p$-shell result from integrating over the appropriate bound-state region of $E_{\rm miss}$ and decompose in a similiar manner save for an additional multiplicative recoil factor given by $f_{\rm recoil} = \left[1 - \frac{E_p}{E_{\rm recoil}}\frac{\vec{P}_{\rm miss}\cdot\vec{p}_p}{p_p^2}\right]$.

[109] The accuracy of the response function separation depends on precisely matching the values of $|\vec{q}|$ and ω at each of the different kinematic settings. This precise matching was achieved by measuring ^{1}H(e,ep) with a pinhole collimator placed in front of the HRS$_e$. The proton momentum was thus $\vec{q}$. The ^{1}H(e,ep) proton momentum peak was determined to $\delta p/p = 1.5 \times 10^{-4}$, which allowed for an identical matching of $\delta|\vec{q}|/|\vec{q}|$ between the different kinematic settings.

[110] $R_{L+TT} \equiv R_L + \frac{V_{TT}}{V_L}R_{TT}$

[111] The nucleon current was calculated using a fully relativistic operator, and the wave functions were four-component spinor solutions of the Dirac equation including scalar and vector potentials.

[112] In contrast to the GK nucleon form factor model preferred by Udías *et al.*, Kelly employs the MMD nucleon form factor model. Differences are small at this Q^2.

[113] The quantity y (which is the minimum value of the initial momentum of the nucleon) is generally used to label non-quasielastic kinematics. According to [1], $y = -\frac{|\vec{q}|}{2} + \frac{m_N\omega}{|\vec{q}|}\sqrt{\frac{\vec{q}\cdot\vec{q}}{Q^2}(1 + \frac{Q^2}{4m_N^2})}$, which for these kinematics, is 0.22. $y = 0$ for quasielastic kinematics.